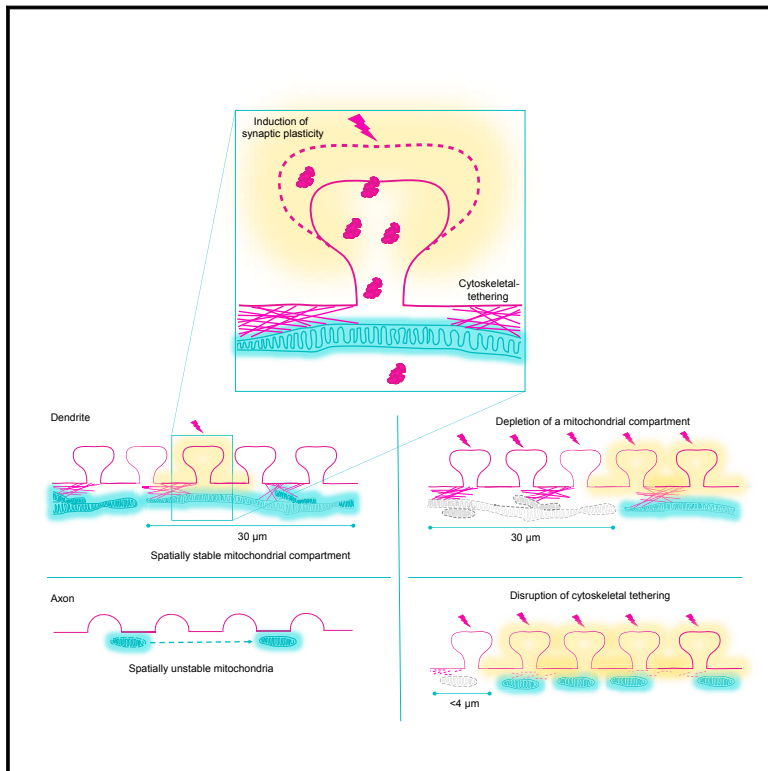# Spatially Stable Mitochondrial Compartments Fuel Local Translation during Plasticity

Graphical Abstract

Authors

Vidhya Rangaraju, Marcel Lauterbach, Erin M. Schuman

Correspondence

erin.schuman@brain.mpg.de

In Brief

Spatially restricted mitochondria fuel the extensive local protein synthesis needed to support synaptic plasticity.

Highlights

- Mitochondria exist in temporally stable spatial ~30 μm compartments in dendrites

- Cytoskeletal tethering determines size and stability of mitochondrial compartments

- Local depletion of mitochondrial compartments affects synaptic plasticity

- Mitochondrial compartments provide energy within spatially confined boundaries

Spatially Stable Mitochondrial Compartments Fuel Local Translation during Plasticity

Vidhya Rangaraju,[1] Marcel Lauterbach,[1,2] and Erin M. Schuman[1,3,*]
[1]Max Planck Institute for Brain Research, Frankfurt 60438, Germany
[2]Present address: Center for Integrative Physiology and Molecular Medicine, Saarland University, Homburg 66421, Germany
[3]Lead Contact
*Correspondence: erin.schuman@brain.mpg.de
https://doi.org/10.1016/j.cell.2018.12.013

SUMMARY

Local translation meets protein turnover and plasticity demands at synapses, however, the location of its energy supply is unknown. We found that local translation in neurons is powered by mitochondria and not by glycolysis. Super-resolution microscopy revealed that dendritic mitochondria exist as stable compartments of single or multiple filaments. To test if these mitochondrial compartments can serve as local energy supply for synaptic translation, we stimulated individual synapses to induce morphological plasticity and visualized newly synthesized proteins. Depletion of local mitochondrial compartments abolished both the plasticity and the stimulus-induced synaptic translation. These mitochondrial compartments serve as spatially confined energy reserves, as local depletion of a mitochondrial compartment did not affect synaptic translation at remote spines. The length and stability of dendritic mitochondrial compartments and the spatial functional domain were altered by cytoskeletal disruption. These results indicate that cytoskeletally tethered local energy compartments exist in dendrites to fuel local translation during synaptic plasticity.

INTRODUCTION

Unlike most other cells, neurons have elaborate morphologies including a few centimeters to meters of cable comprising axons and dendrites. Associated with this is a dramatic increase in cellular volume and the de-centralization of many cell biological processes traditionally associated with the cell somata (Holt and Schuman, 2013; Rangaraju et al., 2017). One prominent example of a de-centralized process is the localization of mRNA and protein synthesis to dendrites and axons. Local translation is a temporally efficient mechanism for activity-dependent proteomic plasticity and can, in principle, allow for the replacement of proteins owing to turnover (Cajigas et al., 2010; Cohen et al., 2013; Dörrbaum et al., 2018; Hanus and Schuman, 2013; Sutton et al., 2006). In addition, local translation, producing many protein copies from a single mRNA, is energetically efficient, considering the energy required to otherwise transport all newly synthesized proteins from the somata to distal ends of dendrites and axons (Schnitzer and Block, 1997) (unpublished calculations).

Glucose is the primary energy fuel, which is oxidized via glycolysis in the cytoplasm and oxidative phosphorylation in mitochondria to generate ATP. In neurons, mitochondria are abundant in all cellular compartments; ~50% of presynaptic terminals possess at least 1 mitochondrion (Shepherd and Harris, 1998) and ~50% of the dendritic length possesses a mitochondrion (Li et al., 2004). In presynaptic terminals, the huge energy demand for presynaptic function is met by activity-driven ATP synthesis originating from both glycolysis and oxidative phosphorylation (Ashrafi and Ryan, 2017; Ashrafi et al., 2017; Jang et al., 2016; Rangaraju et al., 2014). In contrast, in postsynaptic spines and dendrites, very little is known about the link between energy supply and demand (Li et al., 2004; Schuman and Chan, 2004). In addition to maintaining ionic balance, maintaining proteostasis and modifying synaptic proteomes represent a large energy demand. Protein synthesis consumes ~4 ATP molecules per peptide bond formation (Harris and Attwell, 2012; Moldave, 1985); the energy demand is proportional to the length of the macromolecule undergoing synthesis. In the postsynaptic densities of a neuron alone, ~2,670 protein copies are turned over per minute (Cohen et al., 2013). However, it is not clear what fuels the local protein synthesis that is important for some forms of synaptic plasticity (Schuman and Chan, 2004; Steward and Schuman, 2003). Here, we report that spatially stable mitochondrial compartments fuel dendritic translation in an activity-dependent manner during synaptic plasticity.

RESULTS

Protein Synthesis Is Powered by Mitochondria

To examine how protein synthesis is fueled in dendritic compartments, we investigated the two main energy supplies of the cell—glycolysis and mitochondrial respiration. We used the puro-PLA method (tom Dieck et al., 2015) to visualize newly synthesized proteins in dendritic and somatic compartments of cultured hippocampal neurons after a brief (10 min) period of metabolic labeling. We inhibited mitochondrial or glycolytic ATP sources during basal neuronal activity (Figure 1A). Acute treatment of neurons with antimycin or oligomycin, which block complex III or complex V of the mitochondrial electron transport chain, respectively, abolished protein synthesis in both somatic and dendritic compartments (Figures 1B–1E and S1C). On the
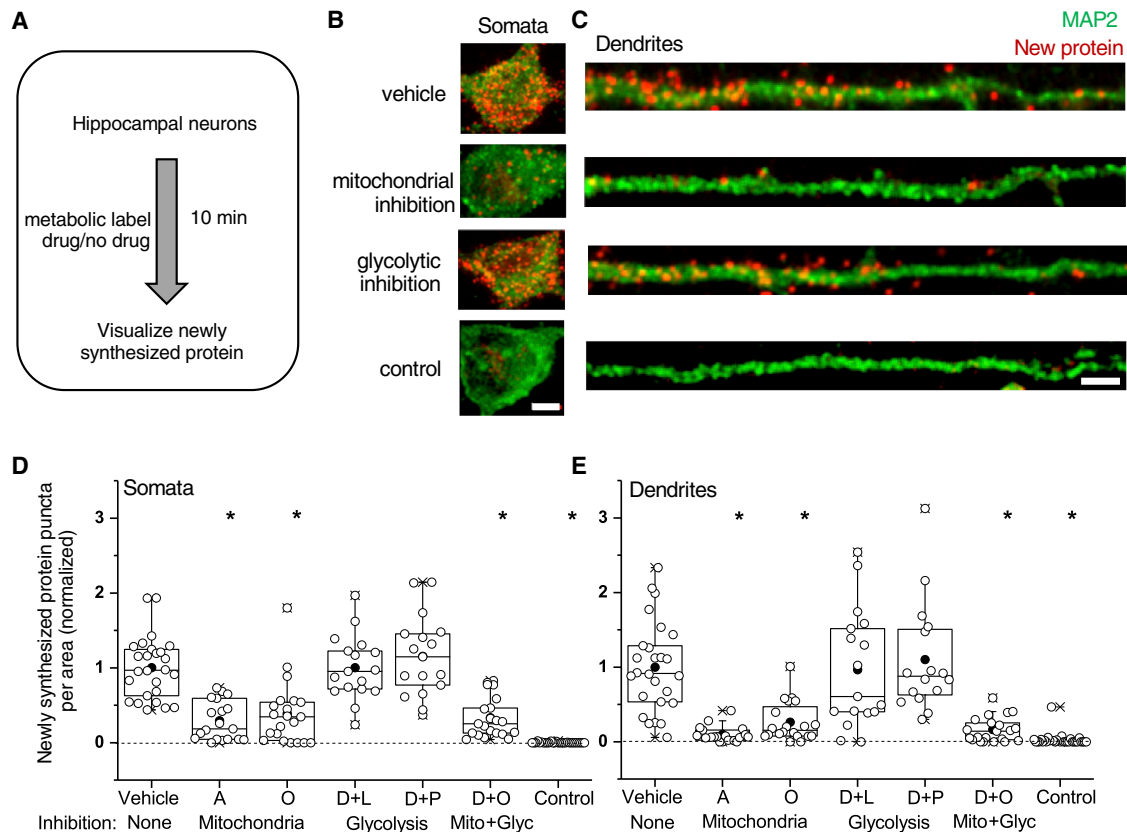
Figure 1. Protein Synthesis Is Powered by Mitochondria, Not Glycolysis

(A) Experimental workflow for visualizing newly synthesized proteins following ATP synthesis inhibition (STAR Methods).

(B and C) Representative images showing newly synthesized protein puncta (red) measured by metabolic labeling with puromycin in somata (B) and dendrites (C). Hippocampal neurons acutely treated for 10 min with drugs to inhibit mitochondrial function (antimycin or oligomycin) exhibited a significant decrease in newly synthesized proteins compared to neurons that were untreated (vehicle) or treated with drugs to inhibit glycolysis (deoxyglucose in the presence of lactate or pyruvate). The absence of puromycin was used as a negative control (control) and MAP2 (green) was used as a dendritic marker. Scale bar, 5 μm.

(D and E) Average number of newly synthesized protein puncta normalized to area measured in various conditions in somata (D) and dendrites (E).

vehicle, antimycin (A), oligomycin (O), deoxyglucose + lactate (D+L), deoxyglucose + pyruvate (D+P), deoxyglucose + oligomycin (D+O), absence of puromycin (control), $n \geq 16$ neurons from 2 animals. One-way ANOVA, Tukey test, *$p < 0.05$.

See also Figure S1.

other hand, inhibition of glycolysis by acute (Figures 1B–1E) or prolonged treatment (Figures S1A and S1B) with deoxyglucose (Wick et al., 1957; Pelicano et al., 2006; Rangaraju et al., 2014) (in the presence of the mitochondrial substrates pyruvate or lactate) did not affect protein synthesis in either compartment. These data indicate that neuronal protein synthesis in both somata and dendrites is powered by mitochondria, and not glycolysis, during basal neuronal activity. In addition, given the brief metabolic labeling period (10 min—associated with limited diffusion of nascent proteins), these data also suggest that the reduced detection of nascent proteins in dendrites represents a requirement for mitochondrial function in local translation—that is explored in greater depth below.

Dendritic Mitochondria Exist in Temporally Stable Spatial Compartments

In neurons, protein synthesis-dependent plasticity occurs on timescales of minutes to hours (Bradshaw et al., 2003; Huber et al., 2000; Kang and Schuman, 1996; Martin et al., 1997; Vickers et al., 2005). To examine further if mitochondria provide fuel for local translation during synaptic plasticity, we measured dendritic mitochondrial dynamics within these timescales. While mitochondrial motility has been measured in dendrites and axons before, these measurements were of relatively short (2–16 min) duration (Fu et al., 2017; Kang et al., 2008; Macaskill et al., 2009; Wang and Schwarz, 2009) or during neuronal development (Faits et al., 2016; Lewis et al., 2016; Smit-Rigter et al., 2016). Using the fluorescence loss in photobleaching (FLIP) method, which measures cell compartment continuity (Lippincott-Schwartz et al., 2003), we examined mitochondrial dynamics in neurons using a mitochondria-targeted DsRed fluorescent protein. Mitochondrial fluorescence, in DsRed-Mito expressing neurons, was repeatedly photobleached at a local region of a dendrite, axon, or soma, during continuous imaging of the whole neuron (Figure 2A). Following 30 min of FLIP, the fluorescence loss in the photobleached region was compared to the
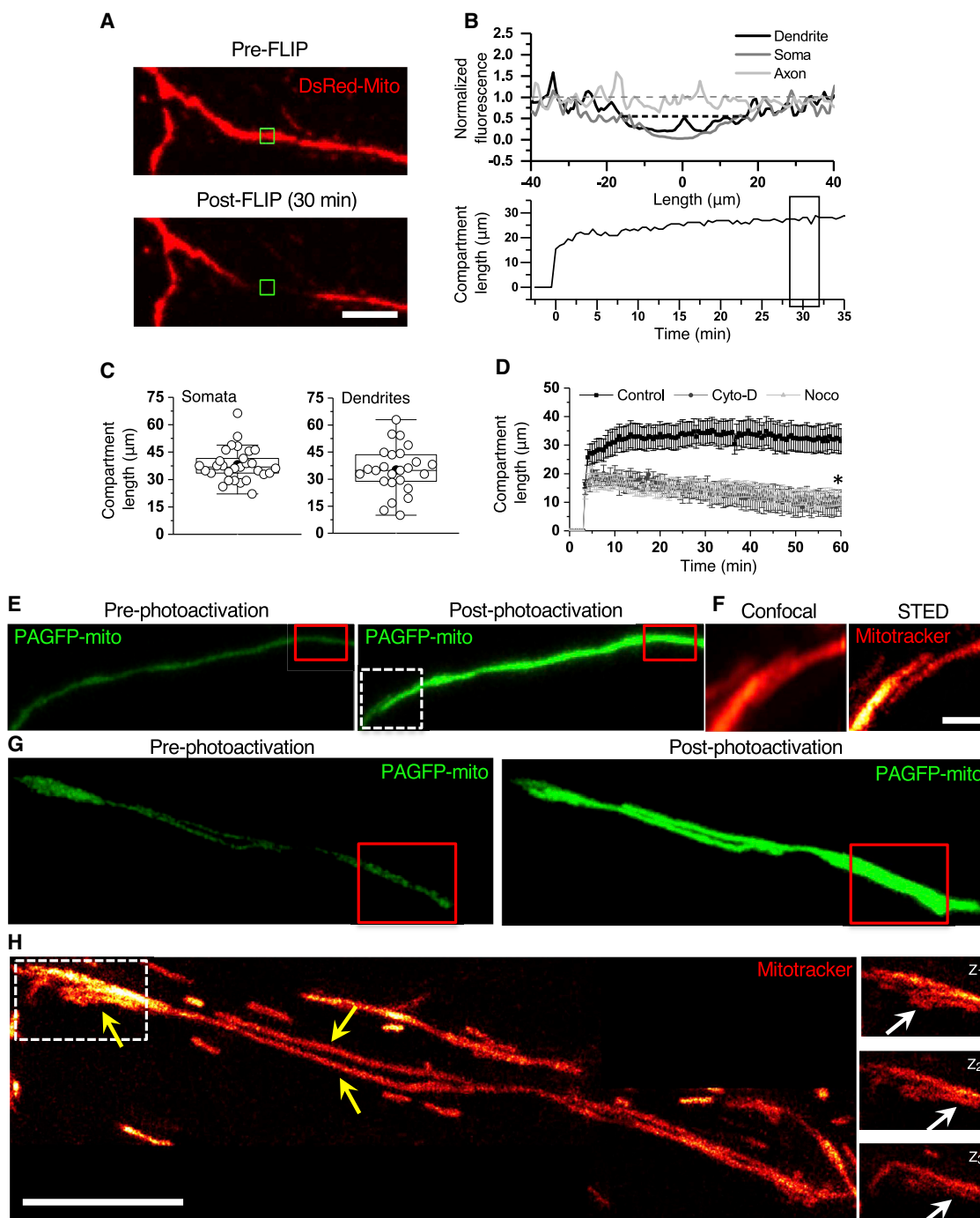
Figure 2. Dendritic Mitochondria Are Temporally Stable Spatial Compartments of Single or Multiple Mitochondrial Filaments Tethered to the Cytoskeleton.

(A) Hippocampal neuron expressing DsRed-Mito (red) before (top) and after (bottom) 30 min FLIP at a proximal dendritic region (green open square). Scale bar, 20 μm.

(B) Top: representative fluorescence line profile measured at the end of 30 min FLIP normalized to pre-FLIP fluorescence (gray dashed line). Normalized fluorescence line profile showing a depression, centered at the site of FLIP, in dendrite (black) and somata (dark gray) but not in axon (light gray). Black dashed line represents the width of the depression at half-height of the minimum—defined as mitochondrial compartment length. Bottom: representative time course of the compartment length shows steady state at 30 min. Black rectangle denotes the time point at which compartment lengths were measured for further analyses.

(C) Average mitochondrial compartment lengths measured in somata (left, n = 29 neurons from 6 animals) and dendrites (right, n = 25 neurons from 5 animals). All data averages are presented as mean ± SEM in the text.

adjacent non-photobleached regions. A spatially restricted decrease in fluorescence was measured in dendrites and somata, revealing the existence of spatially confined compartments of mitochondria (Figure 2B, top; STAR Methods). Notably, these confined mitochondrial compartments were not observed in axons (Figure 2B, top). The dendritic mitochondrial compartments were also stable over time for the duration (30 min) of the experiment (Figures 2B, bottom, and S2B). (Phototoxic effects, such as mitochondrial swelling, were often observed in FLIP experiments longer than 30 min thus preventing us from examining mitochondrial dynamics over even longer time periods). Our measurements revealed an average somatic mitochondrial compartment length of 38 ± 2 μm and an average dendritic mitochondrial compartment length of 35 ± 3 μm (Figure 2C), consistent with previous (static) measurements using electron microscopy (Popov et al., 2005). The length of the mitochondrial compartments was not influenced by the mitochondrial marker used, the size of the FLIP region (Figure S2A) or the measurement temperature (Figure S2B). Mitochondrial compartments were also measured in parallel with two other structures containing membrane, the endoplasmic reticulum (ER) and the plasma membrane (PM). DsRed-Mito expressing neurons co-expressing either ER-targeted GFP or PM-targeted pHluorin (Cui-Wang et al., 2012) were used to perform simultaneous FLIP measurements (Figure S2C; STAR Methods). The mitochondrial compartments were different from both ER and PM compartments (Figures S2C and S2D), as expected given their different respective membrane dynamics.

To investigate the temporal stability of the mitochondrial compartments and to confirm the measured length of these compartments, we used fluorescence photoactivation (Lippincott-Schwartz et al., 2003). Mitochondria were photoactivated either in dendrites or axons of neurons expressing photoactivatable GFP targeted to the mitochondrial matrix (PAGFP-mito) and monitored for 60 min (Figures S2E, S2F, bottom, S2J, left, and S2K, left) (comparable measurements could not be obtained in the soma given its larger volume). The mitochondrial compartment length was measured as the spatial spread of the photoactivated fluorescent signal (STAR Methods). Consistent with the FLIP measurements, mitochondrial compartments of length 31 ± 4 μm were measured that were stable for up to 60 min (Figure 2D). Extending the imaging period to 2 hr revealed relatively stable compartments for up to ∼80 min that began to diminish in size over the next 40 min, presumably owing to turnover, fission, and organelle movement (Figure S2F, top). Mitochondrial compartments were less stable at branch points than in proximal and distal parts of dendrites, consistent with the flux of cargo

and increased transport often observed at branch points (Figures S2G–S2I). In contrast, the mitochondria observed in axons over a similar imaging period were much smaller and very dynamic (Figures S2E, bottom, S2F, bottom, S2K, left, and S2L).

Dendritic Mitochondria Are Regulated by Tethering to the Cytoskeleton

Next, we investigated the molecular mechanisms that influence the stability of the mitochondrial compartments. We perturbed the actin and microtubule network with the depolymerizing agents cytochalasin-D (cyto-D) and nocodazole (noco), respectively, and examined the mitochondrial length and dynamics using PAGFP-mito. Disruption of either the actin- or microtubule-based cytoskeleton significantly reduced the dendritic mitochondrial compartment length, evident within the few minutes of photoactivation (21 ± 2 μm and 18 ± 4 μm, measured at 5 min, for cyto-D and noco, respectively). Not only were the dendritic mitochondrial compartments shortened, they were also destabilized, exhibiting a significant reduction in length over time (9 ± 3 μm and 11 ± 3 μm, measured at 60 min, for cyto-D and noco, respectively; Figures 2D and S2J; STAR Methods). The same experiments conducted in axons revealed that cyto-D and noco yielded the opposite result. Disruption of the cytoskeleton led to dramatic stabilization of the axonal mitochondria (see also Ligon and Steward, 2000) (Figures S2K and S2L) (control 5.1 ± 1.0 μm, cyto-D 4.0 ± 0.6 μm, noco 3.2 ± 0.4 μm at 5 min and control 0.96 ± 0.46 μm, cyto-D 3.8 ± 0.7 μm, noco 2.8 ± 0.4 um at 60 min). These data indicate that the mitochondrial-cytoskeletal interactions are fundamentally different in axons and dendrites. The data also clearly indicate a role for both actin and microtubule filaments in the tethering and stabilization of dendritic mitochondrial compartments.

Dendritic Mitochondrial Compartments Exist as Single or Multiple Mitochondrial Filaments

We investigated the nature of the observed mitochondrial compartments—do they constitute single or multiple mitochondrial filaments? To address this, we made use of stimulated emission depletion (STED) microscopy (Hell, 2007; Hell and Wichmann, 1994) to resolve the mitochondrial compartments in live neurons. Neurons expressing PAGFP-mito were additionally labeled with Mitotracker Deep Red for STED imaging. PAGFP was photoactivated in a region, where an apparent "single" mitochondrial filament was observed (at confocal resolution), and the subsequent spread of the photoactivated GFP—the mitochondrial compartment- was then monitored (Figures 2E and 2G). In addition, the mitochondrial compartment was resolved with STED

(D) Average time course of the photoactivated mitochondrial compartment lengths show stable mitochondria in control dendrites (black, n = 18 dendrites from 1 animal) and destabilized mitochondrial compartments following actin (dark gray, n = 6 dendrites from 1 animal) and microtubule (light gray, n = 12 dendrites from 2 animals) depolymerization. One-way ANOVA at 60 min, Tukey test, *p < 0.0005.

(E–H) Photoactivation of mitochondrial compartments (red rectangle) in PAGFP-mito expressing hippocampal neurons (green) (E and G) constituted either single (F), scale bar 1 μm, or multiple (H), scale bar 5 μm, filaments of mitochondria revealed by live STED imaging using Mitotracker Deep Red (orange) (see STAR Methods).

White dashed box depicts the regions magnified for better visualization (F; H, right inset). The inset shows a mitochondrial filament in three Z sections (Z_1, Z_2, and Z_3) at 330-nm interval showing intermittent contacts (white arrows) with the adjacent mitochondrion. Yellow arrows point to the multiple mitochondrial filaments observed in the STED image of the photoactivated compartment.

See also Figure S2.
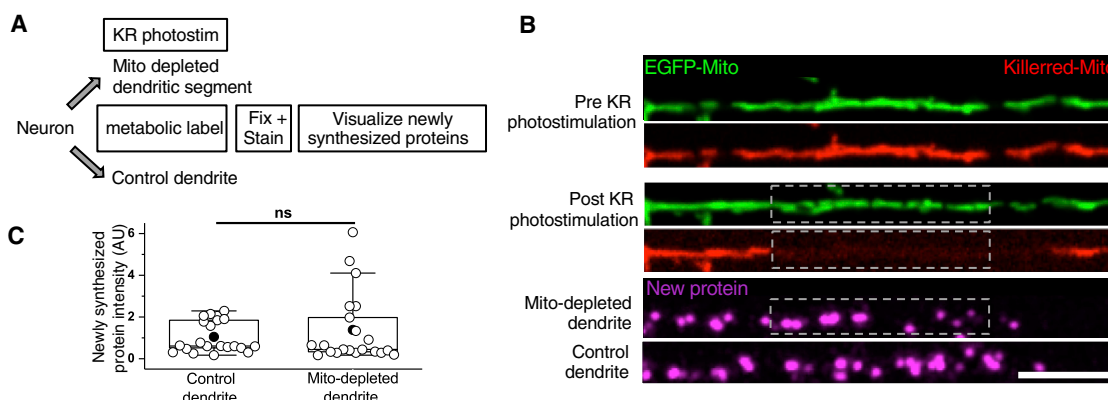
Figure 3. Mitochondrial Compartments Do Not Power Local Translation in Dendrites during Basal Neuronal Activity

(A) Experimental workflow for local mitochondrial depletion in dendrites (STAR Methods).

(B) Top: representative image of a neuronal dendrite transfected with EGP-Mito (green) and Killerred-Mito (red) showing mitochondrial fragmentation and photobleaching of the Killerred (KR) fluorescence following KR photostimulation in the selected region (dashed gray box, middle), performed in the presence of the metabolic label puromycin. Bottom: mitochondria-depleted dendritic region showed no change in newly synthesized protein puncta (new protein, purple) compared to an adjacent non-KR photostimulated control dendrite. Scale bar, 10 μm.

(C) Average newly synthesized protein intensity measured pairwise in non-KR photostimulated control dendrites and KR photostimulated-mitochondria depleted dendrites at various photostimulation conditions (STAR Methods).

n = 21 dendrites from 6 animals, pair-sample t test, p = 0.2.

See also Figure S3.

---

microscopy (Figures 2F and 2H). Analysis of mitochondrial compartments revealed (STAR Methods) two separate groups: (1) single filamentous mitochondrion displaying a distinct gap separating it from adjacent mitochondria at STED resolution and no spread of photoactivated GFP to the adjacent mitochondria (Figures 2E and 2F), and (2) multiple filaments of mitochondria—either with branched filaments or intermittent contacts between filaments—that exhibited spread of photoactivated GFP between them (Figures 2G and 2H). For a total of 29 mitochondrial compartments analyzed, 10 (~34%) were composed of multiple filaments and the rest (19) were single mitochondrial filaments (Figure S2M). These results are consistent with previous (static) mitochondrial observations from electron microscopy (Huang et al., 2013; Popov et al., 2005) and live STORM images from other cells (Shim et al., 2012). Altogether, the above experiments suggest that single or multiple mitochondrial filaments are spatially stabilized at a dendritic region for up to ~80 min, via cytoskeletal anchoring, presumably to fuel protein synthesis and other energy demanding processes.

Mitochondrial Compartments Are Not Required to Power Local Translation during Basal Neuronal Activity

To investigate directly if local mitochondrial compartments provide energy for dendritic translation, we locally depleted the compartments and then measured protein synthesis (Figure 3A). We achieved local inhibition of a mitochondrial compartment optogenetically by targeting the phototoxic protein KillerRed (KR) to the mitochondrial matrix (KillerRed-Mito) (Ashrafi et al., 2014). KillerRed generates reactive oxygen species (ROS) upon photobleaching and causes oxidative stress to nearby molecules (Roy et al., 2010). Spatially restricted (~10–25 μm in length; STAR Methods) Killerred-Mito photostimulation resulted in a corresponding local fragmentation of mitochondria (Figures 3B, mid-

dle, and S3C) (compared to a non-photostimulated control dendrite of the same neuron; Figure S3A), without releasing appreciable ROS in the cytosol (Figure S3D). The fragmentation of mitochondria was only observed within the KR photostimulated segment and not in the corresponding upstream or downstream segments (Figure S3B; STAR Methods). These observations are consistent with the idea that, on average, a single mitochondrial compartment is depleted following KR photostimulation of a ~10–25 μm segment. We assessed the effect of local mitochondrial depletion on protein synthesis using puro-PLA, as described above. Surprisingly, the local inhibition of mitochondrial function by KR photostimulation did not affect protein synthesis measured in the KR-photostimulated region (Figure 3B, bottom). Pairwise comparisons were made either with a non-photostimulated control dendrite of the same neuron (Figures 3B and 3C) or with an adjacent non-photostimulated region of the same dendrite (Figure S3E). Altering the frequency and/or duration of the KR photostimulation and increasing the duration of metabolic labeling did not reveal an effect of mitochondrial inhibition on local translation (Figure S3F). In addition, treatment with deoxyglucose (to block glycolysis) in conjunction with KR photostimulation also did not alter local translation in dendrites (Figure S3G). Therefore, at basal levels of neuronal activity, the energy demands of local translation are adequately met by global ATP levels available in dendrites; the disabling of local mitochondria can be compensated for by ambient ATP levels or ATP produced by neighboring unperturbed mitochondria.

Mitochondrial Compartments Fuel Local Translation during Plasticity

We reasoned that while existing ATP is sufficient to fuel translation during ongoing activity, the enhanced energy demands

associated with synaptic plasticity induction and maintenance might reveal a different picture. For example, high frequency or patterned stimulation can lead to synaptic plasticity that requires local translation (Bradshaw et al., 2003; Govindarajan et al., 2011; Vickers et al., 2005). To test if local mitochondrial compartments fuel protein synthesis during plasticity, we first developed a synaptic stimulation protocol that would induce both morphological plasticity of spines and a consistent increase in local translation. Neurons expressing GCaMP6s and PSD95-mCherry were used for these experiments to monitor the responsiveness and morphology of individual spines. Two-photon uncaging of glutamate (60 pulses; 0.5 Hz) was performed at PSD95-positive spines in the presence of forskolin to activate the PKA pathway and induce long-term structural plasticity (Figure 4A) (Govindarajan et al., 2011). We observed that this protocol led to a reliable and forskolin-dependent long-term increase in the spine-head width and volume (Figures 4B–4D; STAR Methods). We included puromycin to metabolically label newly synthesized proteins (Figures 4A and 4E; STAR Methods) in stimulated spines using different stimulation regimes (Figure S4A; STAR Methods). As with the spine morphological plasticity stimulation protocol, we found that a stimulation frequency of 0.5 Hz with 60 (or 120) pulses was optimal—eliciting robust increases in new protein synthesis within dendritic spines with success rates of 72%–84% (Figures 4F, S4A, and S4B; STAR Methods). In contrast, unstimulated spines measured in the same dendrite or control dendrites failed to exhibit consistent changes in spine morphology: only 29% of the unstimulated spines exhibited translation (Figures 4B–4F). These experiments indicate that local synaptic stimulation of an individual spine results in a long-lasting change in spine morphology as well as an enhanced probability of local translation.

With this optimized uncaging protocol, we next investigated if local mitochondrial compartments are important to fuel the plasticity-induced synaptic translation. Neurons expressing GCaMP6s, PSD95-mCherry, and Killerred-Mito were used for these experiments. Following local inhibition (via KR photostimulation) of a mitochondrial compartment in a dendrite, a spine in the mitochondria-depleted region was stimulated using the above protocol (Figure 5A; STAR Methods). Simultaneously, a spine from a control dendrite was also stimulated with the same protocol. During uncaging, the calcium response measured in KR photostimulated spines was not different from the control spines (Figure S5A). While spine morphological plasticity was observed at the stimulated spine of the control dendrite, it was blocked in the stimulated spine of the mitochondria-depleted dendritic region (Figures 5B–5D). In addition, an absence or a reduction in newly synthesized protein signal was also observed in the mitochondria-depleted spine (Figures 5E and 5F). In control experiments, we used a KillerRed targeted to the peroxisome (KillerRed-Perox). Photostimulation of Killered-Perox did not affect the plasticity-induced synaptic translation (Figures S5B and S5C). Similarly, photostimulation of a simple fluorescent molecule targeted to the mitochondria, Dsred-Mito, did not affect the stimulation-induced synaptic translation (Figure S5D). Taken together, these data are consistent with a specific role of KR in disabling the local mitochondrial compartment. To further confirm that the defects in spine

morphological plasticity and protein synthesis are due to energy failure, we overexpressed the cytosolic form of the brain-type creatine kinase (CKB-OE) that is known to regenerate ATP via the phosphocreatine system (Fukumitsu et al., 2015; Lin et al., 2013). CKB-OE was confirmed by immunostaining (STAR Methods). We observed a partial recovery of protein synthesis: ~56% of CKB-OE mitochondria-depleted spines exhibited protein synthesis compared to 24% of wild-type (WT) mitochondria-depleted spines (Figure 5F). The inability of CKB-OE to completely recover the local energy failure could be due to altered calcium handling in the CKB-OE mitochondria-depleted dendrites (Figure S5A).

The dynamic behavior of mitochondria is also controlled by the processes of fusion and fission. To examine the effect of fission on mitochondrial function in dendrites, we manipulated the mitochondrial fission factor (MFF), a mitochondrial outer-membrane receptor for the GTPase dynamin-related protein 1 (Drp1) that catalyzes mitochondrial fission (Loson et al., 2013; Otera et al., 2010). As previously observed (Toyama et al., 2016), overexpression of MFF (MFF-OE) resulted in a significant shortening of the dendritic mitochondria (control: 27 ± 3 μm, MFF-OE 12 ± 2 μm at 5 min; and control: 31 ± 4 μm, MFF-OE 9 ± 1 μm at 60 min) (Figures S5E and S5F); we also noted a significant but modest reduction in the stability of the mitochondrial compartment (MFF-OE 12 ± 2 μm at 5 min; MFF-OE 9 ± 1 μm at 60 min) (Figures S5F and S5G); this was accompanied by a reduction in the stimulus-elicited intracellular Ca^{2+} signal (Figure S6A). MFF-OE was confirmed by immunostaining (Figure 5G, bottom; STAR Methods). Because MFF-OE alters the size and the stability of the mitochondrial compartment, we used it to examine the importance of these features on plasticity-induced protein synthesis in stimulated spines. We found that MFF-OE negatively affected the success rate of new protein synthesis in stimulated spines (Figures 5G, top, and 5H), suggesting that the size and/or the stability of dendritic mitochondrial compartments is a pre-requisite for plasticity-induced synaptic translation.

Mitochondrial Compartments Fuel Plasticity-Induced Local Translation within Spatially Confined Boundaries

We next tested directly the spatial domain served by a local dendritic mitochondrial compartment, by examining the effects of local mitochondrial depletion on plasticity-induced protein synthesis in neighboring spines. As above, local depletion of a dendritic mitochondrial compartment was performed using KR photostimulation and a spine in the mitochondria-depleted region received a synaptic plasticity-inducing stimulus (Figure 6A). Simultaneously, a spine on the same dendrite, at varying distances from the mitochondria-depleted spine, was also uncaged with the same stimulus (Figure 6A). As before, within the region of KR photostimulation, there was a significantly diminished probability of detecting nascent protein following plasticity induction. Probing different scales of the dendritic neighborhood revealed that stimulated spines that were relatively close (within 0–30 μm) to the mitochondria-depleted region were much less likely to exhibit synaptic translation than "remote" (30–50 μm away) stimulated spines (Figures 6A–6C). To test whether the stability of mitochondrial compartments regulates the size of
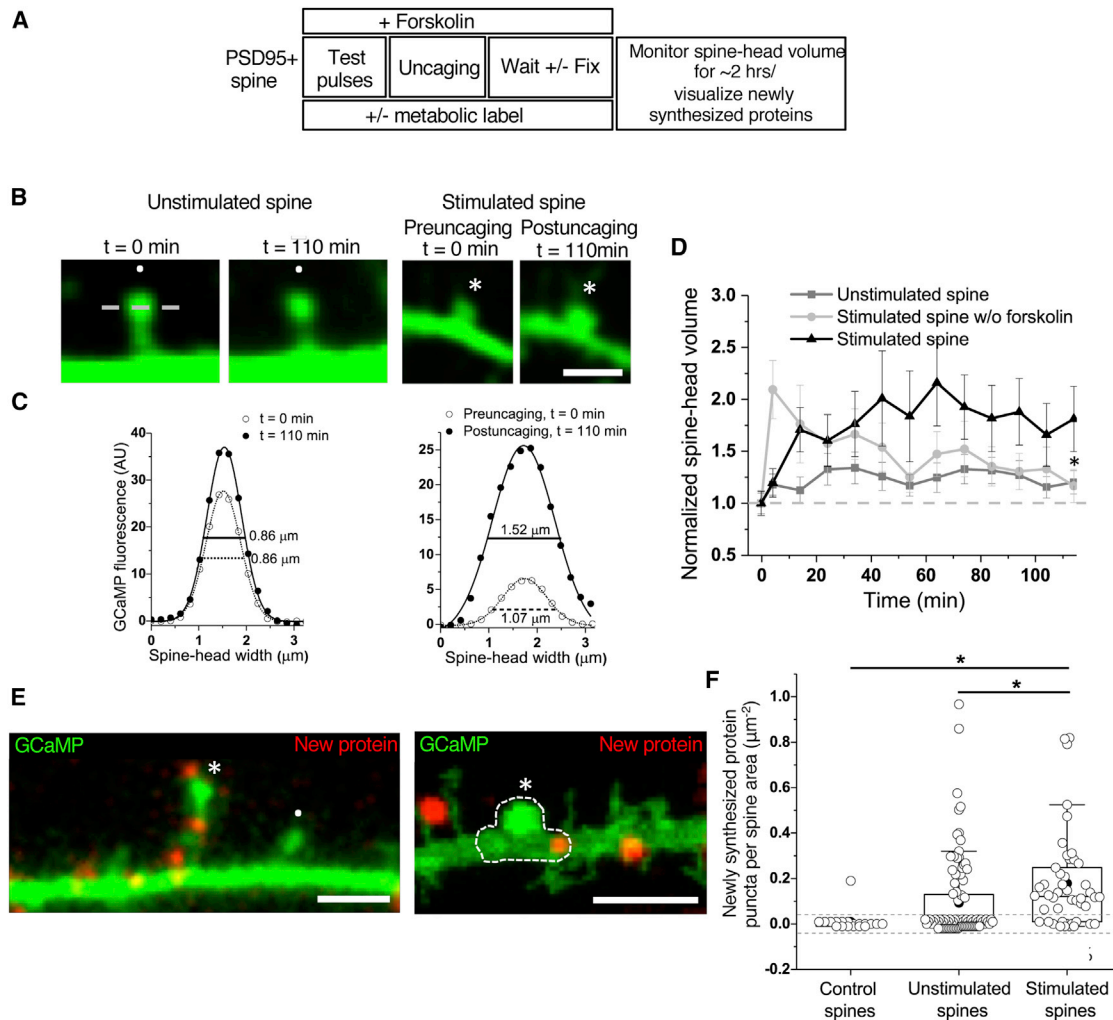
Figure 4. Development of a Synaptic Stimulation Protocol to Induce Spine Morphological Plasticity and Plasticity-Induced Synaptic Translation

(A) Experimental workflow of synaptic stimulation for visualizing spine morphology and newly synthesized proteins (STAR Methods).

(B) Representative unstimulated spine measured at 0 min and 110 min showed no change in spine-head width, whereas the stimulated spine measured at 0 min (pre-uncaging) and 110 min (post-uncaging) showed an increase in spine-head width. Scale bar, 3 μm.

(C) GCaMP fluorescence intensity along the line crossing the center of the spine-head (gray dashed line in B), fit to a Gaussian to measure the full width at the half maximum—the spine-head width (STAR Methods).

(D) Average time course showed a concomitant increase in spine-head volume in stimulated spines, but not in the absence of forskolin or in unstimulated spines, during the period of 110 min. n ≥ 14 spines from 10 animals. One-way ANOVA at 114 min, Tukey test, ***p < 0.0005.

(E) Two representative spines that received a glutamate uncaging stimulus (*) in the presence of the metabolic label puromycin exhibited synaptic translation (new protein, red), whereas an adjacent unstimulated spine (.) did not. Dotted line denotes the synaptic area traced by using the GCaMP signal to measure newly synthesized protein puncta per spine area. Scale bar, 5 μm.

(F) Average number of newly synthesized protein puncta normalized to spine area measured in control (without metabolic labeling), unstimulated, and stimulated spines. 72% of the stimulated spines, and only 29% of the unstimulated spines and 5% of the control spines exhibited synaptic translation. Note that zero values for both stimulated and unstimulated spines were offset by ±0.01 and ±0.02 points to allow visualization of data, enclosed within two dashed gray lines. n ≥ 19 spines from 13 animals, two-sample t test, *p < 0.05.

See also Figure S4.

the affected neighborhood, we perturbed the local cytoskeletal-tethering of mitochondrial compartments using cytochalasin-D. Following actin depolymerization, the stimulated spine within the KR region still exhibited a significantly reduced probability of protein synthesis, but the effect on neighboring stimulated spines was significantly altered (Figure 6B). Spines within

0–30 μm of the KR zone exhibited a likelihood of protein synthesis often similar to control (no KR neighbor) levels. Neither cyto-D nor nocodazole affected the stimulation-induced postsynaptic Ca^{2+} levels (Figure S6A) or baseline measurements of protein synthesis (Figure S6B). These data emphasize the importance of specific features of the mitochondrial compartment, its
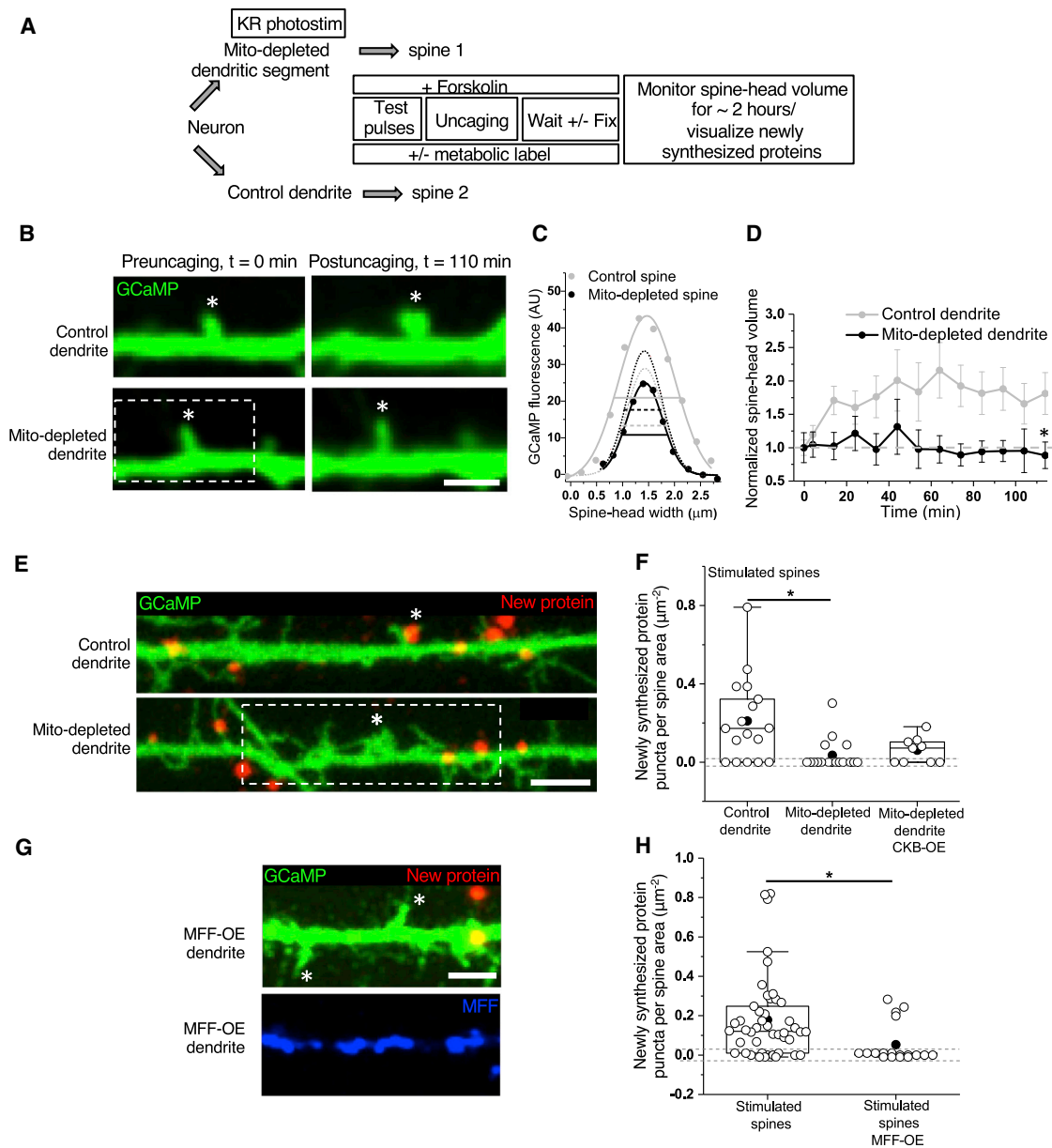
Figure 5. Mitochondrial Compartments Power Local Translation in Dendrites during Synaptic Plasticity

(A) Experimental workflow for spine morphology measurements and synaptic translation following local mitochondrial depletion (STAR Methods).

(B) Increase in spine-head width was not observed in the stimulated spine (*) of the KR photostimulated-mitochondria depleted dendritic region (dashed white box) compared to the stimulated spine (*) of an adjacent non-KR photostimulated control dendrite. Scale bar, 3 μm.

(C) Spine-head width measured in: stimulated spine of the KR photostimulated-mitochondria depleted dendritic region: 0.81 μm (pre-uncaging, t = 0 min), 0.80 μm (post-uncaging, t = 110 min) (black); stimulated spine of an adjacent non-KR photostimulated control dendrite: 0.82 μm (pre-uncaging, t = 0 min), 1.28 μm (post-uncaging, t = 110 min) (gray).

(D) Average time course of spine-head volume measured in stimulated spines of control dendrites (gray, note that data are taken from Figure 4D, stimulated spine) and mitochondria-depleted dendrites (black) normalized to spine-head volume at pre-uncaging, t = 0 min (gray dashed line). n ≥ 15 spines from 8 animals. Two-sample t test, *p < 0.0005.

(E) Synaptic translation (new protein, red) was not observed in the stimulated spine (*) of the KR photostimulated mitochondria-depleted dendritic region (dashed white box) compared to the stimulated spine (*) of an adjacent non-KR photostimulated control dendrite. Note that the new protein puncta visible outside of the GCaMP6s signal arise from adjacent non-transfected neurons or glial cells in the background. Scale bar, 5 μm.

(F) Average number of newly synthesized protein puncta normalized to spine area measured pairwise in stimulated spines of control dendrites and mitochondria-depleted dendrites; and in mitochondria-depleted dendrites overexpressing brain-type creatine kinase (CKB-OE). 71% of the stimulated spines, and only 24% of the mito-depleted stimulated spines exhibited synaptic translation, whereas 56% of the CKB-OE mito-depleted stimulated spines exhibited partial recovery of synaptic translation. Control dendrite and Mito-depleted dendrite n = 17 spines from 7 animals, paired-sample t test, *p < 0.05; control dendrite and

(legend continued on next page)

stability, and its potential size optimization, to fuel cell biological processes like protein synthesis in spatially confined domains (Figure 6C).

DISCUSSION

Using a variety of conventional and super-resolution imaging techniques to image live mitochondria, stimulation of individual synapses using two-photon uncaging, measurement of spine morphological plasticity and metabolic labeling of nascent proteins, we demonstrate the following: (1) mitochondria exist in temporally stable spatial ~30 μm compartments of single or multiple mitochondrial filaments in dendrites; (2) local cytoskeletal-tethering is important for size and stability of mitochondrial compartments (3) under basal conditions mitochondria provide the energy for local dendritic translation; (4) local depletion of mitochondrial compartments affects both spine morphological plasticity and plasticity-induced synaptic translation but not local translation during basal neuronal activity; and (5) mitochondrial compartments serve as local energy reserves with spatially confined boundaries.

Using photoactivation, we measured mitochondrial movement both in dendrites and axons for periods of 60–120 min. We found that dendritic mitochondria exist as stable compartments for up to ~80 min, and axonal mitochondria are, by contrast, much less stable. The observation of motile axonal mitochondria contrasts with previous measurements that were conducted at much shorter (2–16 min) timescales and/or a lower imaging temperature (20°C/room temperature [RT]) (Kang et al., 2008; Wang and Schwarz, 2009). The differences between dendritic and axonal mitochondrial dynamics could arise from the different transport machineries that facilitate mitochondrial distribution in dendrites and axons (van Spronsen et al., 2013). The orientation of microtubules that is crucial for mitochondrial trafficking is also different between dendrites (mix of plus- and minus-end-out) and axons (plus-end-out) (Stone et al., 2008). Interestingly, perturbation of the cytoskeletal architecture by the depolymerization of actin or microtubules exerted opposite effects on the mitochondrial compartments in dendrites and axons. Cytoskeletal perturbation destabilized mitochondrial compartments in dendrites, while it stabilized them in axons (see also Ligon and Steward, 2000). The molecular interaction of mitochondria with its local cytoskeletal structure appears to use different mechanisms in dendrites and axons, suggesting different adaptor proteins or post-translational modifications of the microtubule (Barlan and Gelfand, 2017). For example, syntaphilin is a protein that docks mitochondria to microtubules and is specific only for axonal compartments (Kang et al., 2008). Identifying additional axon versus dendrite-specific adaptor proteins, that govern the interactions of mitochondria with the cytoskeleton, will illuminate the different mechanisms that govern the mitochondrial dynamics in dendrites and axons. Notably the tethering of dendritic mitochondria by the cytoskeleton appears to impose limits on the dendritic compartment subserved by an individual mitochondrial compartment. Blocking the cytoskeletal interaction abbreviated mitochondrial size and stability but also changed the neighborhood plasticity rules, such that the spatial domain over which the mitochondrial function was coordinated (~30 μm) was distorted.

The difference in mitochondrial behavior between dendrites and axons could also reflect the difference in the timescales of the metabolic needs in the two neuronal compartments. While glycolysis and mitochondrial ATP synthesis are the two major ATP producing pathways, the former is optimized for the rate of ATP production, while the latter is optimized for ATP yield (Pfeiffer et al., 2001). Synaptic vesicle trafficking causes the largest metabolic burden in presynaptic terminals and is carried out in the timescale of seconds and is fueled by activity-driven glycolysis along with mitochondrial function (Ashrafi et al., 2017; Jang et al., 2016; Rangaraju et al., 2014). On the other hand, protein translation-dependent synaptic plasticity is carried out on timescales of minutes to hours, well-suited to a mitochondrial source of energy. Careful dissection of the rate and amount of metabolic needs in spines and dendrites, similar to ATP measurement studies in presynaptic terminals (Rangaraju et al., 2014) will shed light on how the morphological and dynamic features of the mitochondria are tuned to their function in specific compartments. In this regard, the striking differences in the size and stability of dendritic and axonal mitochondria may be a good example of "organelle optimization" within the subcellular compartments of an individual cell.

Memory formation is driven by the modification of the local synaptic proteome in response to a synapse-specific stimulus. Here, we show for the first time spine-specific modulation of protein synthesis, using two-photon glutamate uncaging for synapse-specific stimulation and metabolic labeling of nascent proteins in addition to spine morphological plasticity in neuronal cultures. It is, however, not clear how synaptic stimulation signals the need for ATP to drive synaptic translation. The spatially confined nature of the mitochondrial compartments suggests a signal that could exhibit local increase following synaptic activity, such as Ca^{2+} (Rangaraju et al., 2014), which in turn could activate mitochondrial compartments spanning ~30 μm of dendritic length for local ATP synthesis and subsequent energy provision for 30–300 spines (1–10 spines/μm) (Hering and Sheng, 2001).

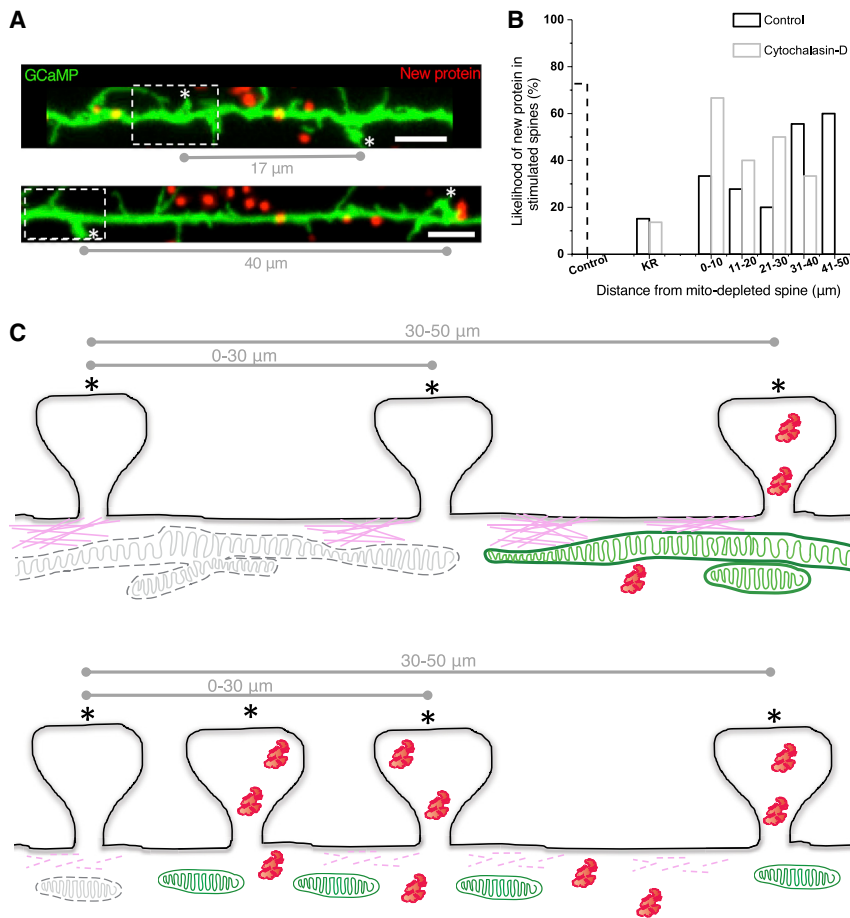
Mito-depleted dendrite with CKB-OE n ≥ 9 spines from 4 animals, two-sample t test, p = 0.05. Zero values for all three conditions are enclosed within two dashed gray lines.

(G) Synaptic translation (new protein, red) was not observed in the stimulated spines (*) of dendrites overexpressing the mitochondrial fission factor (MFF-OE) (top), confirmed by immunostaining (bottom) (MFF, blue). Scale bar, 5 μm.

(H) Average number of newly synthesized protein puncta normalized to spine area measured in stimulated spines of control dendrites and MFF-OE dendrites. 72% of the control stimulated spines (note that data are taken from Figure 4F, stimulated spines), and only 26% of the MFF-OE stimulated spines exhibited synaptic translation. Note that zero values for both control and MFF-OE stimulated spines were offset by ±0.01 points to allow visualization of data, enclosed within two dashed gray lines.

n ≥ 18 spines from 2 animals, two-sample t test, *p < 0.05.

See also Figure S5.

A

GCaMP New protein

17 μm

40 μm

B

Likelihood of new protein in stimulated spines (%)

Control
Cytochalasin-D

100
80
60
40
20
0

Control   KR   0-10 11-20 21-30 31-40 41-50

Distance from mito-depleted spine (μm)

C

30-50 μm
0-30 μm

* * *

30-50 μm
0-30 μm

* * * *

Figure 6. Mitochondrial Compartments Fuel Plasticity-Induced Local Translation within Spatially Confined Boundaries

(A) Top: representative stimulated spine 17 μm away from the mitochondria-depleted (white dashed box) spine did not exhibit synaptic translation (new protein, red), whereas a stimulated spine that was 40 μm away (bottom) from the mitochondria-depleted spine exhibited synaptic translation. Note that new protein puncta visible outside of the GCaMP6s signal arise from adjacent non-transfected neurons or glial cells in the background. Scale bar, 5 μm.

(B) Histogram showing higher likelihood of nascent protein detection in stimulated spines within 0–30 μm from mitochondria-depleted spines in control dendrites (black) (KR, n = 43; 0–10, n = 6; 11–20, n = 9; 21–30, n = 10; 31–40, n = 9; 41–50, n = 5, n represents spines from 12 animals); following actin depolymerization, the effect of mitochondria-depletion on neighboring stimulated spines was significantly altered—spines within 0–30 μm of the KR zone exhibited a likelihood of protein synthesis often similar to control (gray) (KR, n = 11; 0–10, n = 6; 11–20, n = 10; 21–30, n = 6; 31–40, n = 9; 41–50, n = 2, n represents spines from 4 animals). Dashed bar corresponds to likelihood of new protein in stimulated spines taken from Figure 4F.

(C) Illustration showing the significance of spatially stable mitochondrial compartments to fuel local translation in spines following a synaptic stimulation (*). Top: local perturbation of mitochondrial compartments abolishes plasticity-induced synaptic translation, while it does not affect ongoing translation during basal neuronal activity. Mitochondrial compartments (green mitochondria) spatially stabilized by cytoskeletal-tethering (pink actin filaments) serve as local energy reserves with spatially confined boundaries. Local depletion of a mitochondrial compartment (gray mitochondria) only affected plasticity-induced synaptic translation (red proteins) in neighboring stimulated spines (within 0–30 μm) from the mitochondria-depleted region, but did not affect stimulated spines at "remote" distances from the mitochondria-depleted spine (30–50 μm). Bottom: the stability of the mitochondrial compartments regulates its spatial domain of energy provision. Perturbation of cytoskeletal-tethering of mitochondrial compartments using cytochalasin-D (dashed pink actin strands) resulted in shortening and destabilization of the mitochondrial compartments (short green mitochondria). Local depletion of a perturbed mitochondrial compartment (gray short mitochondria) altered the spatial domain affected. Neighboring spines within 0–30 μm, and "remote" spines 30–50 μm, from the mitochondria-depleted spine exhibited plasticity-induced synaptic translation. These data emphasize the importance of the specific features of the mitochondrial compartment, its stability, and its potential size optimization, in fueling plasticity-induced synaptic translation. Note that microtubules are not shown in this illustration.

See also Figure S6.

Given the limited diffusion of ATP (Hubley et al., 1996), the existence of the local energy reserves with spatially confined boundaries we describe here is essential.

Mitochondria remain one of the least understood cellular organelles (Harbauer, 2017), and a surprising convergence of sequencing studies (Couvillion et al., 2016) and mitochondriopathies (Sheng and Cai, 2012) indicate that mitochondrial function and dysfunction are hotspots for regulation. In parallel, the synapse (Grant, 2012) and local translation (Wang et al., 2016) have emerged repeatedly as focal points for dysregulation in disease. However, a detailed understanding of the relationships between local translation, energy metabolism and neuronal activity is lacking. Here, we show local depletion of mitochondrial energy compartments results in severe impairment of plasticity-induced synaptic translation and spine morphological plasticity opening up a new set of unexplored questions regarding synaptic plasticity and metabolism. Understanding these interactions could lead to new therapeutic targets of neurodevelopmental disorders resulting from protein synthesis impairment and mitochondrial dysfunction.

STAR★METHODS

Detailed methods are provided in the online version of this paper and include the following:

- KEY RESOURCES TABLE
- CONTACT FOR REAGENT AND RESOURCE SHARING
- EXPERIMENT MODEL AND SUBJECT DETAILS
  - Cell culture preparation, Transfection and Imaging

- ● METHOD DETAILS
  - ○ Constructs
  - ○ Optical Measurements
  - ○ FLIP experiments
  - ○ Photoactivation experiments
  - ○ STED experiments
  - ○ Uncaging experiments
  - ○ Spine-head volume measurement
  - ○ Killerred experiments
  - ○ Mitochondria fragmentation measurement
  - ○ Cytosolic reactive oxygen species measurement
  - ○ Newly synthesized protein (Puro-PLA) labeling
  - ○ ATP synthesis inhibition
- ● QUANTIFICATION AND STATISTICAL ANALYSIS

REFERENCES

Ashrafi, G., and Ryan, T.A. (2017). Glucose metabolism in nerve terminals. Curr. Opin. Neurobiol. 45, 156–161.

Ashrafi, G., Schlehe, J.S., LaVoie, M.J., and Schwarz, T.L. (2014). Mitophagy of damaged mitochondria occurs locally in distal neuronal axons and requires PINK1 and Parkin. J. Cell Biol. 206, 655–670.

Ashrafi, G., Wu, Z., Farrell, R.J., and Ryan, T.A. (2017). GLUT4 mobilization supports energetic demands of active synapses. Neuron 93, 606–615.

Barlan, K., and Gelfand, V.I. (2017). Microtubule-based transport and the distribution, tethering, and organization of organelles. Cold Spring Harb. Perspect. Biol. 9, a025817.

Bradshaw, K.D., Emptage, N.J., and Bliss, T.V. (2003). A role for dendritic protein synthesis in hippocampal late LTP. Eur. J. Neurosci. 18, 3150–3152.

Cajigas, I.J., Will, T., and Schuman, E.M. (2010). Protein homeostasis and synaptic plasticity. EMBO J. 29, 2746–2752.

Chen, T.W., Wardill, T.J., Sun, Y., Pulver, S.R., Renninger, S.L., Baohan, A., Schreiter, E.R., Kerr, R.A., Orger, M.B., Jayaraman, V., et al. (2013). Ultrasensitive fluorescent proteins for imaging neuronal activity. Nature 499, 295–300.

Cohen, L.D., Zuchman, R., Sorokina, O., Müller, A., Dieterich, D.C., Armstrong, J.D., Ziv, T., and Ziv, N.E. (2013). Metabolic turnover of synaptic proteins: kinetics, interdependencies and implications for synaptic maintenance. PLoS ONE 8, e63191.

Contreras, L., Drago, I., Zampese, E., and Pozzan, T. (2010). Mitochondria: the calcium connection. Biochim. Biophys. Acta 1797, 607–618.

Couvillion, M.T., Soto, I.C., Shipkovenska, G., and Churchman, L.S. (2016). Synchronized mitochondrial and cytosolic translation programs. Nature 533, 499–503.

Cui-Wang, T., Hanus, C., Cui, T., Helton, T., Bourne, J., Watson, D., Harris, K.M., and Ehlers, M.D. (2012). Local zones of endoplasmic reticulum complexity confine cargo in neuronal dendrites. Cell 148, 309–321.

Dörrbaum, A.R., Kochen, L., Langer, J.D., and Schuman, E.M. (2018). Local and global influences on protein turnover in neurons and glia. eLife 7, e34202.

Faits, M.C., Zhang, C., Soto, F., and Kerschensteiner, D. (2016). Dendritic mitochondria reach stable positions during circuit development. eLife 5, e11583.

Fu, Z.X., Tan, X., Fang, H., Lau, P.M., Wang, X., Cheng, H., and Bi, G.Q. (2017). Dendritic mitoflash as a putative signal for stabilizing long-term synaptic plasticity. Nat. Commun. 8, 31.

Fukumitsu, K., Fujishima, K., Yoshimura, A., Wu, Y.K., Heuser, J., and Kengaku, M. (2015). Synergistic action of dendritic mitochondria and creatine kinase maintains ATP homeostasis and actin dynamics in growing neuronal dendrites. J. Neurosci. 35, 5707–5723.

Govindarajan, A., Israely, I., Huang, S.Y., and Tonegawa, S. (2011). The dendritic branch is the preferred integrative unit for protein synthesis-dependent LTP. Neuron 69, 132–146.

Grant, S.G. (2012). Synaptopathies: diseases of the synaptome. Curr. Opin. Neurobiol. 22, 522–529.

Hanus, C., and Schuman, E.M. (2013). Proteostasis in complex dendrites. Nat. Rev. Neurosci. 14, 638–648.

Hanus, C., Geptin, H., Tushev, G., Garg, S., Alvarez-Castelao, B., Sambandan, S., Kochen, L., Hafner, A.S., Langer, J.D., and Schuman, E.M. (2016). Unconventional secretory processing diversifies neuronal ion channel properties. Elife 5.

Harbauer, A.B. (2017). Mitochondrial health maintenance in axons. Biochem. Soc. Trans. 45, 1045–1052.

Harris, J.J., and Attwell, D. (2012). The energetics of CNS white matter. J. Neurosci. 32, 356–371.

Hell, S.W. (2007). Far-field optical nanoscopy. Science 316, 1153–1158.

Hell, S.W., and Wichmann, J. (1994). Breaking the diffraction resolution limit by stimulated emission: stimulated-emission-depletion fluorescence microscopy. Opt. Lett. 19, 780–782.

Hering, H., and Sheng, M. (2001). Dendritic spines: structure, dynamics and regulation. Nat. Rev. Neurosci. 2, 880–888.

Holt, C.E., and Schuman, E.M. (2013). The central dogma decentralized: new perspectives on RNA function and local translation in neurons. Neuron 80, 648–657.

Huang, X., Sun, L., Ji, S., Zhao, T., Zhang, W., Xu, J., Zhang, J., Wang, Y., Wang, X., Franzini-Armstrong, C., et al. (2013). Kissing and nanotunneling mediate intermitochondrial communication in the heart. Proc Natl Acad Sci U S A 110, 2846–2851.

Huber, K.M., Kayser, M.S., and Bear, M.F. (2000). Role for rapid dendritic protein synthesis in hippocampal mGluR-dependent long-term depression. Science 288, 1254–1257.

Hubley, M.J., Locke, B.R., and Moerland, T.S. (1996). The effects of temperature, pH, and magnesium on the diffusion coefficient of ATP in solutions of physiological ionic strength. Biochim. Biophys. Acta 1291, 115–121.

Ivashchenko, O., Van Veldhoven, P.P., Brees, C., Ho, Y.S., Terlecky, S.R., and Fransen, M. (2011). Intraperoxisomal redox balance in mammalian cells: oxidative stress and interorganellar cross-talk. Mol. Biol. Cell 22, 1440–1451.

Jang, S., Nelson, J.C., Bend, E.G., Rodríguez-Laureano, L., Tueros, F.G., Cartagenova, L., Underwood, K., Jorgensen, E.M., and Colón-Ramos, D.A. (2016). Glycolytic enzymes localize to synapses under energy stress to support synaptic function. Neuron 90, 278–291.

Kang, H., and Schuman, E.M. (1996). A requirement for local protein synthesis in neurotrophin-induced hippocampal synaptic plasticity. Science 273, 1402–1406.

Kang, J.S., Tian, J.H., Pan, P.Y., Zald, P., Li, C., Deng, C., and Sheng, Z.H. (2008). Docking of axonal mitochondria by syntaphilin controls their mobility and affects short-term facilitation. Cell 132, 137–148.

Karbowski, M., Arnoult, D., Chen, H., Chan, D.C., Smith, C.L., and Youle, R.J. (2004). Quantitation of mitochondrial dynamics by photolabeling of individual organelles shows that mitochondrial fusion is blocked during the Bax activation phase of apoptosis. J. Cell Biol. 164, 493–499.

Lewis, T.L., Jr., Turi, G.F., Kwon, S.K., Losonczy, A., and Polleux, F. (2016). Progressive decrease of mitochondrial motility during maturation of cortical axons in vitro and in vivo. Curr. Biol. 26, 2602–2608.

Li, Z., Okamoto, K., Hayashi, Y., and Sheng, M. (2004). The importance of dendritic mitochondria in the morphogenesis and plasticity of spines and synapses. Cell 119, 873–887.

Ligon, L.A., and Steward, O. (2000). Role of microtubules and actin filaments in the movement of mitochondria in the axons and dendrites of cultured hippocampal neurons. J. Comp. Neurol. 427, 351–361.

Lin, Y.S., Cheng, T.H., Chang, C.P., Chen, H.M., and Chern, Y. (2013). Enhancement of brain-type creatine kinase activity ameliorates neuronal deficits in Huntington's disease. Biochim. Biophys. Acta 1832, 742–753.

Lippincott-Schwartz, J., Altan-Bonnet, N., and Patterson, G.H. (2003). Photobleaching and photoactivation: following protein dynamics in living cells. Nat. Cell Biol. (Suppl), S7–S14.

Loson, O.C., Song, Z., Chen, H., and Chan, D.C. (2013). Fis1, Mff, MiD49, and MiD51 mediate Drp1 recruitment in mitochondrial fission. Mol Biol Cell 24, 659–667.

Macaskill, A.F., Rinholm, J.E., Twelvetrees, A.E., Arancibia-Carcamo, I.L., Muir, J., Fransson, A., Aspenstrom, P., Attwell, D., and Kittler, J.T. (2009). Miro1 is a calcium sensor for glutamate receptor-dependent localization of mitochondria at synapses. Neuron 61, 541–555.

Martin, K.C., Casadio, A., Zhu, H., Yaping, E., Rose, J.C., Chen, M., Bailey, C.H., and Kandel, E.R. (1997). Synapse-specific, long-term facilitation of aplysia sensory to motor synapses: a function for local protein synthesis in memory storage. Cell 91, 927–938.

Matsuzaki, M., Honkura, N., Ellis-Davies, G.C., and Kasai, H. (2004). Structural basis of long-term potentiation in single dendritic spines. Nature 429, 761–766.

Moldave, K. (1985). Eukaryotic protein synthesis. Annu. Rev. Biochem. 54, 1109–1149.

Otera, H., Wang, C.X., Cleland, M.M., Setoguchi, K., Yokota, S., Youle, R.J., and Mihara, K. (2010). Mff is an essential factor for mitochondrial recruitment of Drp1 during mitochondrial fission in mammalian cells. Journal of Cell Biology 191, 1141–1158.

Pelicano, H., Martin, D.S., Xu, R.H., and Huang, P. (2006). Glycolysis inhibition for anticancer treatment. Oncogene 25, 4633–4646.

Pfeiffer, T., Schuster, S., and Bonhoeffer, S. (2001). Cooperation and competition in the evolution of ATP-producing pathways. Science 292, 504–507.

Popov, V., Medvedev, N.I., Davies, H.A., and Stewart, M.G. (2005). Mitochondria form a filamentous reticular network in hippocampal dendrites but are present as discrete bodies in axons: a three-dimensional ultrastructural study. J. Comp. Neurol. 492, 50–65.

Rangaraju, V., Calloway, N., and Ryan, T.A. (2014). Activity-driven local ATP synthesis is required for synaptic function. Cell 156, 825–835.

Rangaraju, V., Tom Dieck, S., and Schuman, E.M. (2017). Local translation in neuronal compartments: how local is local? EMBO Rep 18, 693–711.

Roy, A., Carpentier, P., Bourgeois, D., and Field, M. (2010). Diffusion pathways of oxygen species in the phototoxic fluorescent protein KillerRed. Photochem. Photobiol. Sci 9, 1342–1350.

Sambandan, S., Akbalik, G., Kochen, L., Rinne, J., Kahlstatt, J., Glock, C., Tushev, G., Alvarez-Castelao, B., Heckel, A., and Schuman, E.M. (2017). Activity-dependent spatially localized miRNA maturation in neuronal dendrites. Science 355, 634–637.

Schindelin, J., Rueden, C.T., Hiner, M.C., and Eliceiri, K.W. (2015). The ImageJ ecosystem: an open platform for biomedical image analysis. Mol. Reprod. Dev. 82, 518–529.

Schnitzer, M.J., and Block, S.M. (1997). Kinesin hydrolyses one ATP per 8-nm step. Nature 388, 386–390.

Schuman, E., and Chan, D. (2004). Fueling synapses. Cell 119, 738–740.

Sheng, Z.H., and Cai, Q. (2012). Mitochondrial transport in neurons: impact on synaptic homeostasis and neurodegeneration. Nat. Rev. Neurosci. 13, 77–93.

Shepherd, G.M., and Harris, K.M. (1998). Three-dimensional structure and composition of CA3–>CA1 axons in rat hippocampal slices: implications for presynaptic connectivity and compartmentalization. J. Neurosci. 18, 8300–8310.

Shim, S.H., Xia, C., Zhong, G., Babcock, H.P., Vaughan, J.C., Huang, B., Wang, X., Xu, C., Bi, G.Q., and Zhuang, X. (2012). Super-resolution fluorescence imaging of organelles in live cells with photoswitchable membrane probes. Proc. Natl. Acad. Sci. USA 109, 13978–13983.

Smit-Rigter, L., Rajendran, R., Silva, C.A., Spierenburg, L., Groeneweg, F., Ruimschotel, E.M., van Versendaal, D., van der Togt, C., Eysel, U.T., Heimel, J.A., et al. (2016). Mitochondrial dynamics in visual cortex are limited in vivo and not affected by axonal structural plasticity. Curr. Biol. 26, 2609–2616.

Steward, O., and Schuman, E.M. (2003). Compartmentalized synthesis and degradation of proteins in neurons. Neuron 40, 347–359.

Stone, M.C., Roegiers, F., and Rolls, M.M. (2008). Microtubules have opposite orientation in axons and dendrites of Drosophila neurons. Mol. Biol. Cell 19, 4122–4129.

Sutton, M.A., Ito, H.T., Cressy, P., Kempf, C., Woo, J.C., and Schuman, E.M. (2006). Miniature neurotransmission stabilizes synaptic function via tonic suppression of local dendritic protein synthesis. Cell 125, 785–799.

Taylor, J. (1997). An Introduction to Error Analysis: the Study of Uncertainties in Physical Measurements, Second Edition (University Science Books).

Thévenaz, P., and Unser, M. (2007). User-friendly semiautomated assembly of accurate image mosaics in microscopy. Microsc. Res. Tech. 70, 135–146.

tom Dieck, S., Kochen, L., Hanus, C., Heumüller, M., Bartnik, I., Nassim-Assir, B., Merk, K., Mosler, T., Garg, S., Bunse, S., et al. (2015). Direct visualization of newly synthesized target proteins in situ. Nat. Methods 12, 411–414.

Toyama, E.Q., Herzig, S., Courchet, J., Lewis, T.L., Jr., Losón, O.C., Hellberg, K., Young, N.P., Chen, H., Polleux, F., Chan, D.C., and Shaw, R.J. (2016). Metabolism. AMP-activated protein kinase mediates mitochondrial fission in response to energy stress. Science 351, 275–281.

van Spronsen, M., Mikhaylova, M., Lipka, J., Schlager, M.A., van den Heuvel, D.J., Kuijpers, M., Wulf, P.S., Keijzer, N., Demmers, J., Kapitein, L.C., et al. (2013). TRAK/Milton motor-adaptor proteins steer mitochondrial trafficking to axons and dendrites. Neuron 77, 485–502.

Vickers, C.A., Dickson, K.S., and Wyllie, D.J. (2005). Induction and maintenance of late-phase long-term potentiation in isolated dendrites of rat hippocampal CA1 pyramidal neurones. J. Physiol. 568, 803–813.

Wang, X., and Schwarz, T.L. (2009). The mechanism of Ca2+-dependent regulation of kinesin-mediated mitochondrial motility. Cell 136, 163–174.

Wang, E.T., Taliaferro, J.M., Lee, J.A., Sudhakaran, I.P., Rossoll, W., Gross, C., Moss, K.R., and Bassell, G.J. (2016). Dysregulation of mRNA localization and translation in genetic disease. J. Neurosci. 36, 11418–11426.

Wick, A.N., Drury, D.R., Nakada, H.I., and Wolfe, J.B. (1957). Localization of the primary metabolic block produced by 2-deoxyglucose. J. Biol. Chem. 224, 963–969.

STAR★METHODS

KEY RESOURCES TABLE

REAGENT or RESOURCE	SOURCE	IDENTIFIER
Antibodies		
Mouse monoclonal anti-Puromycin	Kerafast	Cat# Equation 0001; RRID: AB_2620162
Guinea pig polyclonal anti-MAP2	Synaptic systems	Cat# 188004; RRID: AB_2138181
Rabbit polyclonal anti-GFP	Abcam	Cat# ab 290; RRID: AB_303395
Rabbit polyclonal anti-MFF	Proteintech	Cat# 17090-1-AP; RRID: AB_2142463
Rabbit polyclonal anti-V5	Sigma	Cat# V8137; RRID: AB_261889
Chicken polyclonal anti-GFP	AVES	Cat# 1020; RRID: AB_10000240
Goat polyclonal anti-guinea pig Dylight 405	Jackson Immuno Research	Cat# 106-475-003; RRID: AB_2337432
Goat polyclonal anti-rabbit Alexa 488	Invitrogen	Cat# A11008; RRID: AB_143165
Goat polyclonal anti-rabbit Alexa 405	Invitrogen	Cat# A31556; RRID: AB_221605
Goat polyclonal anti-chicken Alexa 488	Invitrogen	Cat# A11039; RRID: AB_142924
Chemicals, Peptides, and Recombinant Proteins		
Cytochalasin-D	Sigma	Cat# C8273
Nocodazole	Sigma	Cat# M1404
Mitotracker Deep Red FM	Life Technologies	Cat# M22426
Combimag	OZ biosciences	Cat# CM20100
Lipofectamine	Invitrogen	Cat# 11668027
Tetrodotoxin	Tocris Bioscience	Cat# 1069
Forskolin	Tocris Bioscience	Cat# 1099
Puromycin dihydrochloride	Sigma	Cat# P8833
MNI caged glutamate	Tocris Bioscience	Cat# 1490
DCF (2," 7"-Dichlorofluorescein diacetate)	Sigma	Cat# D6883
Duolink *In Situ* Detection Reagents FarRed	Sigma	Cat# DUO92013
Antimycin A	Enzo lifesciences	Cat# ALX-380-075-M005
Oligomycin	Sigma	Cat# O4876
2-Deoxyglucose	Sigma	Cat# D8375
Pyruvate	Sigma	Cat# P5280
Lactate	Sigma	Cat# L7022
Experimental Models: Organisms/Strains		
Sprague-Dawley rats (Male and female)	Charles River	RRID: RGD_734476
Recombinant DNA		
Killerred-Mito plasmid	Evrogen	Cat# FP964
DsRed-Mito plasmid	Clontech	Cat# 632421
ER-VSVG-GFP plasmid	Cui-Wang et al., 2012	N/A
PM-pHluorin plasmid	Cui-Wang et al., 2012	N/A
PSD95-mCherry plasmid	Hanus et al., 2016	N/A
Killerred-Perox plasmid	Ivashchenko et al., 2011	N/A
MFF-OE plasmid	Toyama et al., 2016	N/A
CKB-OE plasmid	Lin et al., 2013	N/A
PAGFP-mito plasmid	Karbowski et al., 2004	Addgene plasmid 23348

(Continued on next page)

REAGENT or RESOURCE	SOURCE	IDENTIFIER
GCaMP6s plasmid	Chen et al., 2013	Addgene plasmid 40753
EGFP-Mito	This paper	N/A
Software and Algorithms		
Slidebook 5.5	Intelligent Imaging Innovations	https://www.intelligent-imaging.com/slidebook; RRID: SCR_014300
ImageJ	Schindelin et al., 2015	https://ncmir.ucsd.edu/downloads/montagimo_plugins.shtm; RRID: SCR_001935
OriginPro 2017 64Bit	OriginLab	http://www.originlab.com/index.aspx?go=PRODUCTS/Origin; RRID: SCR_014212
MATLAB	Mathworks	https://www.mathworks.com/products/matlab/; RRID: SCR_001622
Imaris	Bitplane	http://www.bitplane.com/imaris/imaris; RRID: SCR_007370
Imspector Software	Abberior instruments	https://www.abberior-instruments.com/products/expert-line/imspector-software/; RRID: SCR_015249

CONTACT FOR REAGENT AND RESOURCE SHARING

Further information and requests for resources and reagents should be directed to and will be fulfilled by the Lead Contact, Erin M. Schuman (erin.schuman@brain.mpg.de).

EXPERIMENT MODEL AND SUBJECT DETAILS

All hippocampal neurons were derived from P0 (postnatal day 0) Sprague-Dawley rat pups (CD® Crl:CD, both male and female, RRID: RGD_734476). Pregnant females from timed matings were delivered from Charles River Laboratories as SPF (Specific-Pathogen Free) animals and housed in the institute's animal facility for one week at a 12/12 hour light dark cycle with food and water *ad libitum* until the litter was born. Pups were killed by decapitation. The housing and sacrificing procedures involving animal treatment and care were conducted in conformity with the institutional guidelines that are in compliance with national and international laws and policies (DIRECTIVE 2010/63/EU; German animal welfare law; FELASA guidelines), under the supervision of the institute's animal welfare officer. The animals were euthanized according to annex 2 of § 2 Abs. 2 Tierschutz-Versuchstier-Verordnung. Animal numbers were reported to the local governmental authority (Regierungspräsidium Darmstadt).

Cell culture preparation, Transfection and Imaging

Hippocampal regions were dissected and dissociated with 2.6 mM L-cysteine-papain (Roth) and 300 μL 2X crystallized papain in dissociation medium (82 mM Na_2SO_4, 30 mM K_2SO_4, 5.8 mM $MgCl_2$, 0.252 mM $CaCl_2$, 1 mM HEPES, 20 mM Glucose, 0.001% phenol red) for 15 minutes at 37°C and triturated with Neuronal Growth Medium (NGM) (GIBCO). Unless specified otherwise, all reagents were purchased from Sigma and all stock solutions were stored at −20°C. Cells were plated on poly-D-lysine coated coverslips mounted on Mattek dishes at a density of 20,000-40,000 cells/cm^2. Cultures were maintained in conditioned neuronal growth medium (NGM) (80% NGM, 15% Glial preparation medium, 5% cortical preparation medium) at 37°C and 5% CO_2. Transfections were performed 12 days after plating by magnetofection using Combimag (OZ biosciences) and Lipofectamine 2000 (Invitrogen) according to manufacturer's instructions. Live cell imaging was conducted between 13-15 days (17 days for Killerred-Perox experiments) after plating. All experiments, unless specified, were performed at a temperature of 32 °C in E4 imaging buffer containing (mM) 120 NaCl, 3 KCl, 10 HEPES (buffered to pH 7.4), 3 $CaCl_2$, 1 $MgCl_2$, and 10 Glucose. For uncaging experiments, modified E4 buffer lacking $MgCl_2$ with 4mM $CaCl_2$ was used –the rest of the constituents remained unchanged.

METHOD DETAILS

Constructs

Killerred-Mito (Evrogen) and DsRed-Mito (Clontech) were purchased and then DsRed was replaced with EGFP to make the EGFP-Mito construct by Rangaraju V in the lab of Ryan TA. ER-VSVG-GFP, PM-pHluorin, PSD95-mCherry constructs were obtained from Hanus C (Cui-Wang et al., 2012; Hanus et al., 2016); Killerred-Perox was obtained from Fransen M (Ivashchenko et al., 2011); MFF-OE was obtained from Lewis TL (Toyama et al., 2016); CKB-OE was obtained from Chern Y (Lin et al., 2013). PAGFP-mito (Karbowski et al., 2004) and GCaMP6s (Chen et al., 2013) were purchased from Addgene (plasmids 23348, 40753 respectively).

Optical Measurements

Live cell imaging was performed using an inverted spinning disk confocal microscope (3i imaging systems; model CSU-X1) using the Slidebook 5.5 software. Images were acquired with a Plan-Apochromat 20x/0.8 DIC objective at laser powers 1.3 mW (488 nm) and 1.4 mW (561 nm) for FLIP experiments; and Plan-Apochromat 63x/1.4 Oil DIC objective at laser powers 1.1 mW (488 nm) and 0.8 mW (561 nm) for Photoactivation, Uncaging, Killerred and DCF experiments, using an Evolve 512 camera (Photometrics). 488 nm excitation and 525/30 nm emission filters were used for PAGFP-mito, GCaMP6s, EGFP-mito, ER-VSVG-GFP, PM-pHluorin and DCF fluorescence; 561 nm excitation and 617/73 nm emission filters were used for Dsred-Mito, Killerred-Mito, Killerred-Perox, and PSD95-mCherry fluorescence. Images were analyzed using ImageJ, unless specified otherwise. OriginPro 2017 was used for data analysis, statistical testing and plotting graphs.

FLIP experiments

A custom-written automated program was used for simultaneous imaging of up to 4 neurons, per dish, with a z stack interval of 1 μm spanning a total of 5 μm. Dual imaging of either ER-VSVG-GFP and Dsred-Mito or PM-pHluorin and Dsred-Mito; or single imaging of EGFP-Mito were performed at laser exposure times 100-200 ms for 488 nm and 2-10 ms for 561 nm. A 5X5 μm² photobleaching spot was chosen either at a soma, dendrite or axon. Images were acquired every 30 s for 40 min. Following the acquisition of pre-FLIP fluorescence images for the first 5 time frames (2.5 min), repeated photobleaching at every time frame was performed with 100 ms pulse duration per pixel and 1.3 μW power of 488 nm laser. In the case of dual imaging, the intensity of the 488 nm laser was sufficient to photobleach the red fluorescent reporter (Dsred-Mito) in addition to the green fluorescent reporters (ER-VSVG-GFP, PM-pHluorin).

For analysis of FLIP experiments, maximum intensity projection images were used. A 0.67 μm (1 pixel) wide segmented line was drawn along the dendrite, axon or soma of interest, inclusive of the 5 μm photobleached spot, ± 60 μm upstream and downstream. A kymograph was generated along the line profile and a custom-written MATLAB (Mathworks, Natick, MA, USA) script was used to extract the data. The script was used to normalize the fluorescence measured along the line profile to the preFLIP fluorescence, find the fluorescence minimum at every time point and calculate the corresponding compartment length at the half height of the minimum. The compartment length measured at the 30th min was used for successive data analyses.

Photoactivation experiments

A custom-written automated program was used for simultaneous imaging of up to 10 neurons, per dish, with a z stack interval of 1 μm spanning a total of 5 μm, with both 488 nm and 561 nm lasers at exposure times of 15 ms. Neurons were transfected with PAGFP-mito and Dsred-Mito plasmid constructs (along with MFF plasmid for MFF-OE experiments). Transfected neurons were identified using Dsred-Mito fluorescence. Photoactivation was performed either in the absence or presence of 25 μg/ml cytochalasin-D (12.5 mg/ml stock made in DMSO) or 10 μg/ml nocodazole (5 mg/ml stock made in DMSO) using a multi-photon laser set-up at 805 nm (Chameleon, Coherent) and a Pockels cell (Conoptics) for controlling the photoactivation pulse. A 5X2 – 10X2 μm² photoactivation spot was chosen either at a dendrite or axon. Images were acquired every 30 s for 70 (or 130) min. Following an acquisition of pre-photoactivation fluorescence images for the first 6 time frames (3 min) a photoactivation pulse was given at the 7th time frame at 1 ms duration per pixel and 3.5 mW power and the imaging continued.

For analysis of photoactivation experiments, images were converted to maximum intensity projections and analyzed by Imaris 8.4.1. Using the 'surface segmentation wizard', the photoactivated mitochondrial region was selected, excluding the non-photoactivated background, by setting a manual threshold. The 'compartment length' was defined as the photoactivated mitochondria extracted across all the time points using the 'filament wizard' and the subsequent addition of the photoactivated mitochondrial filaments, detected above the set threshold during the imaging period. 'Stable compartments' were defined when the measured compartment length stayed constant throughout the imaging period. 'Destabilization of the compartments' were defined when the measured compartment length decreased during the imaging period, corresponding to either movement of the photoactivated mitochondria away from the field of view or the exchange of fluorescence signal between photoactivated mitochondria and non-photoactivated mitochondria resulting in a reduced fluorescence signal that could not be detected above the set threshold.

STED experiments

Live-cell STED imaging was performed using an inverted-STED microscope (Abberior Instruments, Göttingen, Germany) controlled by the Imspector Software. Images were acquired with a 100X 1.4 NA oil immersion objective (Olympus UPlanSApo) with lateral resolution of ∼230 nm for confocal imaging and ∼60 nm resolution for STED imaging. The following excitation and emission wavelengths were used: 485 nm excitation with a 525/50 nm emission filter for PAGFP-mito; 561 nm excitation with a 615/20 nm emission filter for Dsred-Mito; 645 nm excitation with a 685/70 nm emission filter for Mitotracker Deep Red FM (Life Technologies). Neurons were transfected with PAGFP-mito and Dsred-Mito plasmid constructs. Before imaging, neurons were incubated with 200 nM Mitotracker Deep Red FM (1 mM stock made in DMSO) for 15–30 s at room temperature and washed in E4 buffer. Transfected neurons were identified using Dsred-Mito signal. Dendritic regions surrounded by Mitotracker stained glial mitochondria or neighboring neuronal mitochondria were avoided. Photoactivation was performed by scanning the dendritic region of interest using a 485 nm laser with 150 μs pixel dwell time per 80 nm pixel and 10 μW power. For STED super-resolution imaging of the Mitotracker Deep Red channel a depletion wavelength of 775 nm with 15 mW power was used.

Images were linearly deconvolved (Wiener filtered) using a custom-written MATLAB script. For the representative image in Figure 2H, two adjacent images were deconvolved, respective maximum intensity projections obtained and stitched using the ImageJ plugin MosaicJ (Thévenaz and Unser, 2007).

Uncaging experiments

Neurons were transfected with GCaMP6s and PSD95-mCherry plasmid constructs (along with MFF plasmid for MFF-OE experiments). Transfected neurons were identified by change in GCaMP6s fluorescence corresponding to calcium transients in dendrites and spines. PSD95-mCherry fluorescence was used to identify spines for glutamate uncaging. Before glutamate uncaging, neurons were replaced with 1 μM TTX (Citrate salt, 2 mM stock made in water), 50 μM Forskolin (Tocris Bioscience, 100 mM stock made in DMSO), 3 μM Puromycin (92 mM stock made in water), 2 mM 4-Methoxy-7-nitroindolinyl-caged-L-glutamate (MNI caged glutamate) (Tocris Bioscience, 100 mM stock made in E4 buffer) in modified E4 buffer lacking Mg^{2+} (see above). Absence of puromycin was used as control. Glutamate uncaging was performed using a multiphoton-laser 720 nm (Chameleon, Coherent) and a Pockels cell (Conoptics) for controlling the uncaging pulses. Spines that were at least 50 μm away from the cell body were chosen for uncaging experiments. To test a spine's response to an uncaging pulse, an uncaging spot (∼2 μm^2) close to a spine-head was selected and two to three uncaging pulses at 10 ms pulse duration per pixel and 2.5 mW power were given and checked for spine-specific calcium transients. An uncaging protocol of 60 (or 120) uncaging pulses at 0.5 Hz with 10 ms pulse duration per pixel, at 2.5 mW power was used. Following uncaging, neurons were waited for 3 (or 8) min, adding up to a total of 5 (or 10) min of puromycin incubation, and washed with modified E4 buffer. Neurons were fixed in PFA-sucrose (4% PFA, 4% sucrose in PBS-MC) for 15 min, washed in PBS-MC, stored either for 3-4 hours at room temperature (or at 4°C overnight) and continued with the Puro-PLA protocol (see below).

Spine-head volume measurement

To measure changes in spine morphology, uncaging was performed in the absence of the metabolic label puromycin. The omission of forskolin was used as a control. Following the same glutamate-uncaging protocol as above: 60 uncaging pulses at 0.5 Hz with 10 ms pulse duration per pixel, at 2.5 mW power, images were acquired every 10 min for up to 110 min. Using a custom-written MATLAB script, ten images from each time point were averaged and a line crossing the center of the spine-head was drawn. The fluorescence intensity measured along the line was fit to a Gaussian to obtain the full width at half maximum –defined as the spine-head width (Matsuzaki et al., 2004). Spine-head width was converted to spine-head volume, under the assumption that the spine-head is spherical. The uncertainty of the spine-head width measurement was determined from standard error of the mean and was converted to the uncertainty of the spine-head volume by standard error propagation (Taylor, 1997).

Killerred experiments

Neurons were transfected with GCaMP6s and Killerred-Mito plasmid constructs. Killerred-Mito was replaced with Killerred-Perox or Dsred-Mito in control experiments (Figures S5B–S5D), the rest of the protocol remained the same. Transfected neurons were identified by change in GCaMP6s fluorescence corresponding to calcium transients in dendrites and spines. A 10X1 μm^2 – 25X1 μm^2 photostimulation spot was chosen on a dendritic mitochondrial compartment. For Killerred (KR) experiments performed at basal neuronal activity, a photostimulation protocol of 180 pulses at 0.2 Hz (or 20 pulses at 0.03 Hz), with 10 ms pulse duration per pixel at 6.2 μW, 561 nm laser power was given. Neurons were treated with 3 μM puromycin either during the photostimulation protocol or after for 15 min. Following KR photostimulation, neurons were either directly fixed (as explained above) or waited for 20 min before fix.

For KR experiments followed by synaptic stimulation by glutamate uncaging, neurons were transfected with GCaMP6s and KR-Mito (along with CKB plasmid for CKB-OE experiments), in addition to PSD95-mCherry to identify spines for uncaging. Both KR-Mito and PSD95-mCherry were chosen to be red fluorescent reporters as the two additional imaging channels, deep red and blue, were to be used for imaging newly synthesized proteins and MAP2 (or CKB) respectively -described in the Puro-PLA protocol (see below). A 10X1 μm^2 – 25X1 μm^2 photostimulation spot was chosen on a dendritic mitochondrial compartment and a photostimulation protocol of 180 pulses at 0.2 Hz with 10 ms pulse duration per pixel at 6.2 μW, 561 nm laser power was given. Following KR photostimulation, neurons were replaced with the modified E4 buffer for uncaging (as explained above) and a glutamate uncaging protocol of 60 (or 120) uncaging pulses at 0.5 Hz with 10 ms pulse duration per pixel, at 2.5 mW power was given. Fragmentation of the mitochondria was used as a positive readout for efficient perturbation of mitochondrial function (Ashrafi et al., 2014). Spines that did not show a calcium response following KR photostimulated-mitochondria depletion were not included in subsequent analyses. Following uncaging, neurons were waited for 3 min (or 8 min), adding up to a total of 5 (or 10) min of puromycin incubation, washed with modified E4 buffer and fixed (as explained above).

Mitochondria fragmentation measurement

Neurons were transfected with EGFP-Mito and KR-Mito plasmid constructs. Transfected neurons were identified by EGFP-Mito fluorescence in dendrites. A 10X1 μm^2 – 25X1 μm^2 photostimulation spot was chosen on a dendritic mitochondrial compartment. KR photostimulation was performed using the protocol of 180 pulses at 0.2 Hz (or 20 pulses at 0.03 Hz), with 10 ms pulse duration per pixel at 6.2 μW, 561 nm laser power. Simultaneously EGFP-Mito fluorescence was imaged to monitor mitochondrial morphology. An adjacent non-KR photostimulated dendritic region at the same distance from the cell body, as the KR photostimulation region, was used as control.

For mitochondria fragmentation data analysis, the EGFP-Mito dendritic region of interest (KR photostimulated/control) was straightened, set to a manual threshold to remove background fluorescence, and the number of mitochondria particles during the KR photostimulation/control imaging period was analyzed using ImageJ. The number of mitochondria particles measured during the time course of the KR photostimulation/control imaging period was normalized to the number of mitochondria particles measured in the pre-KR photostimulation/control period to calculate the fold increase in mitochondria particles.

To measure the size of the mitochondrial compartment length depleted by KR photostimulation, the dendritic region was binned into three 30 μm segments i) the 30 μm segment encompassing the KR photostimulated region ("photostimulation segment"), ii) 30 μm segment upstream (toward the cell body) of the KR photostimulation segment ("upstream segment") and the iii) 30 μm segment downstream (toward the dendritic tip) of the KR photostimulation segment ("downstream segment"). Mitochondrial fragmentation was measured in photostimulation, upstream and downstream segments as explained above.

Cytosolic reactive oxygen species measurement

Neurons transfected with KR-Mito plasmid construct were stained with 5 μM DCF (2'',7''-Dichlorofluorescein Diacetate) (5 mM stock prepared in DMSO), made in E4 buffer, for 10 min at 37 °C. DCF fluorescence is dependent on the reactive oxygen species (ROS) levels in a cell. Transfected neurons were identified by KR-Mito fluorescence in dendrites. A 10X1 μm^2 – 25X1 μm^2 photostimulation spot was chosen on a dendritic mitochondrial compartment. KR photostimulation was performed (either in the presence or absence of antimycin) using the protocol of 180 pulses at 0.2 Hz, with 10 ms pulse duration per pixel at 6.2 μW, 561 nm laser power. Simultaneously DCF fluorescence was imaged to monitor cytosolic ROS levels. An adjacent non-KR photostimulated dendrite was used as control. Towards the end of photostimulation, the neurons were treated with 40 μM antimycin (40 mM stock made in DMSO), as a positive control for the detection of increase in cytosolic ROS levels by D*CF.*

For cytosolic ROS measurement data analysis, DCF fluorescence measured from the dendritic region of interest (KR photostimulated/control) was background subtracted and analyzed over the time course of the KR photostimulation/control period followed by antimycin treatment. DCF fluorescence measured during KR photostimulation/control period was normalized to the pre-KR photostimulation/control period.

Newly synthesized protein (Puro-PLA) labeling

Fixed neurons were permeabilized (0.5% Triton X-100 in PBS-MC for 15 min), blocked in blocking buffer (4% goat serum in PBS for 1 h) and incubated with ms anti-Puromycin antibody (Kerafast Equation 0001, 1:2500) overnight at 4°C. Unlike using antibody pairs to visualize a specific newly synthesized protein of interest, only Puromycin antibody was used to visualize all newly synthesized proteins. PLA probes ms PLA^{plus} and ms PLA^{minus} were used for the puro-PLA procedure as described previously (Sambandan et al., 2017; tom Dieck et al., 2015) and a far-red fluorescence-labeled oligo was used for detection (Duolink Detection Reagents FarRed). Cells were post-fixed for 10 min at room temperature in PFA-sucrose, washed with PBS-MC and processed further for immunocytochemistry. Neurons were blocked with 4% goat serum in PBS for 1 h followed by incubation with the primary antibody anti-MAP2 gp (SYSY 188004, 2:1000), a dendritic marker, and anti-GFP rb (abcam ab290, 1:1000), for GCaMP6s immunoamplification, for 1.5 h. Neurons were washed in PBS-MC and fluorophore-coupled secondary antibodies anti-gp Dylight 405 (Jackson ImmunoResearch 106-475-003, 2:1000) and anti-rb Alexa 488 (Invitrogen A11008, 1:1000) were incubated for 1 h to detect MAP2 and GCaMP6s respectively. To asses MFF/CKB overexpression, primary antibody anti-MFF rb (Proteintech 17090-1-AP, 1:100) or anti-V5 rb (Sigma V8137, 1:500) (CKB construct was fused with a V5 tag) was used along with anti-GFP chk (AVES 1020, 1:1000), for GCaMP6s immunoamplification, for 1.5 h. Neurons were washed in PBS-MC and fluorophore-coupled secondary antibodies anti-rb Alexa 405 (Invitrogen A31556, 1:500) and anti-chk Alexa 488 (Invitrogen A11039, 1:1000) were incubated for 1 h to detect MFF/CKB and GCaMP6s respectively. Samples were either imaged directly or after storing at 4°C overnight.

Images were acquired with an LSM 880 confocal microscope (Zeiss) using a C-Apochromat 40x/1.2 W objective and a pinhole size of 1 airy unit. Images were acquired in 16-bit mode as Z stacks, with a pixel pitch of 208 nm and field of view of 212.55 X 212.55 μm^2, throughout the entire thickness of the neuron with an optical slice thickness 0.5 μm and pixel dwell times of 0.5 μs. The detector gain in each channel was adjusted to cover the full dynamic range, avoiding saturated pixels. Imaging conditions were kept constant within a batch of experiments. Maximum intensity projections were used for image analyses.

For glutamate uncaging experiments, the shape of the uncaged spine was traced using the GCaMP6s signal (PSD95-mCherry could not be used as mCherry signal got photobleached during KR photostimulation), including the dendritic shaft ± 1 μm upstream and downstream. The number of newly synthesized protein puncta within the traced spine area was counted manually and the newly synthesized protein puncta per spine area was calculated. For unstimulated spine measurements, PSD95-mCherry positive spines were chosen from the same imaging field (up to 7 spines per field), either at least 10 μm away from the uncaged spine on the same dendrite or an adjacent dendrite.

For KR experiments during basal neuronal activity, a 6.2 μm (30 pixels) wide segmented line was drawn at the region of KR photostimulation and the newly synthesized protein intensity along the line was measured. Another line of similar length and width was drawn on an adjacent dendrite, at the same distance from the cell body, to measure the newly synthesized protein intensity in a non-KR photostimulated control dendrite. Both the measured newly synthesized protein intensities were background subtracted before further analyses.

ATP synthesis inhibition

Neurons transfected with EGFP-Mito were used. Transfected dishes were treated with 3 μM puromycin for 10 min (or 20 and 30min) with one of the following: i) 40 μM Antimycin or 1 μM Oligomycin (1 mM stock made in 100% Ethanol) for mitochondrial ATP synthesis inhibition or ii) 10 mM Deoxyglucose replaced for 10 mM glucose in E4, with 5 mM HEPES to compensate for the addition of 5 mM pyruvate (sodium salt) or 5 mM lactate (sodium salt) for glycolysis inhibition or iii) the combination of i and ii for complete ATP synthesis block. E4 buffer in the presence of puromycin was used as a positive control experiment (vehicle) and the absence of puromycin was used as a negative control experiment (control). Following the treatment, neurons were fixed and the puro-PLA protocol (Duolink Detection Reagents Red) was conducted as described above. Cells were post-fixed and processed further for immunocytochemistry as described above with the primary antibody anti-MAP2 gp as a dendritic marker and anti-GFP rb for EGFP-Mito amplification. Secondary antibodies anti-gp Dylight 405 and anti-rb Alexa 488 were used to detect MAP2 and EGFP-Mito, respectively.

Images were acquired using LSM 880 as described above. From each dish of an experimental condition, up to 12 neurons were imaged. A custom-written ImageJ macro was used to concatenate maximum intensity projections of the MAP2 and EGFP-Mito images along with the individual z-slices of the puro-PLA images. From each of these concatenated neurons, the soma was cropped and the individual (one to six) dendrites were traced using a 6.2 μm (30 pixel) segmented line and straightened. Using a custom-written MATLAB script the number of newly synthesized protein puncta was counted in each of the puro-PLA z-slices and summed up in correspondence to the individual soma or dendrite. The image acquired in the absence of puromycin (control) was used to set the threshold for the size and intensity of the newly synthesized protein puncta detected by the script. The threshold parameters were kept constant for each batch of experiments. The measured number of newly synthesized protein puncta was normalized to the corresponding somatic or dendritic area. Individual dendrites belonging to the same neuron were averaged.

## QUANTIFICATION AND STATISTICAL ANALYSIS

Statistical details of experiments including statistical tests used, n and p values can be found in their respective figure legends. In all the figures, the box whisker plots represent the median (line), mean (point), 25th-75th percentile (box), 10th-90th percentile (whisker), 1st–99th percentile (X), and min-max (_) ranges. For all statistical tests, a p value of less than 0.05 was considered significant.
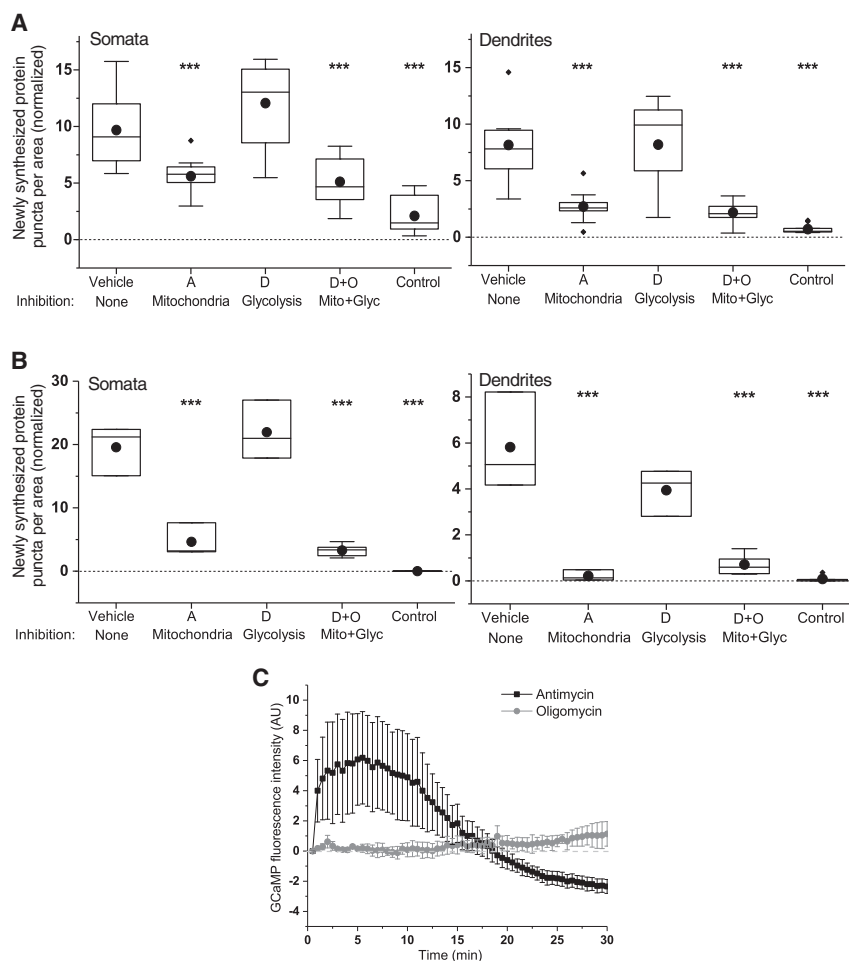
Figure S1. Basal Levels of Dendritic Protein Synthesis Are Not Affected by Glycolytic Inhibitors, Related to Figure 1

(A and B) Average number of newly synthesized protein puncta normalized to area measured in hippocampal neurons treated with various conditions for 20 min (A) or 30 min (B) in somata (left) and dendrites (right): vehicle, Antimycin (A), Deoxyglucose (D), Deoxyglucose+Oligomycin (D+O), absence of puromycin (control), n $\geq$ 3 neurons from 2 animals, One-Way ANOVA, Tukey test, *p < 0.05. Note the increase in the newly synthesized protein puncta per area with increase in the metabolic labeling period (see also Figures 1D and 1E).

(C) Antimycin blocks Complex III of the electron transport chain and depolarizes the mitochondrial membrane potential. It is known that mitochondrial calcium uptake is driven by the mitochondrial membrane potential (Contreras et al., 2010). To examine whether the defect in protein synthesis observed following antimycin treatment is due to reduced mitochondrial calcium buffering, we used an alternative inhibitor of mitochondrial ATP synthesis, Oligomycin, which doesn't affect mitochondrial membrane potential or cytosolic calcium. GCaMP fluorescence measured in neuronal dendrites showed an increase in cytosolic calcium in the presence of antimycin (n = 4 dendrites from 1 animal, black), but not in the presence of oligomycin (n = 3 dendrites from 1 animal, gray), compared to the baseline cytosolic calcium (dashed gray line).
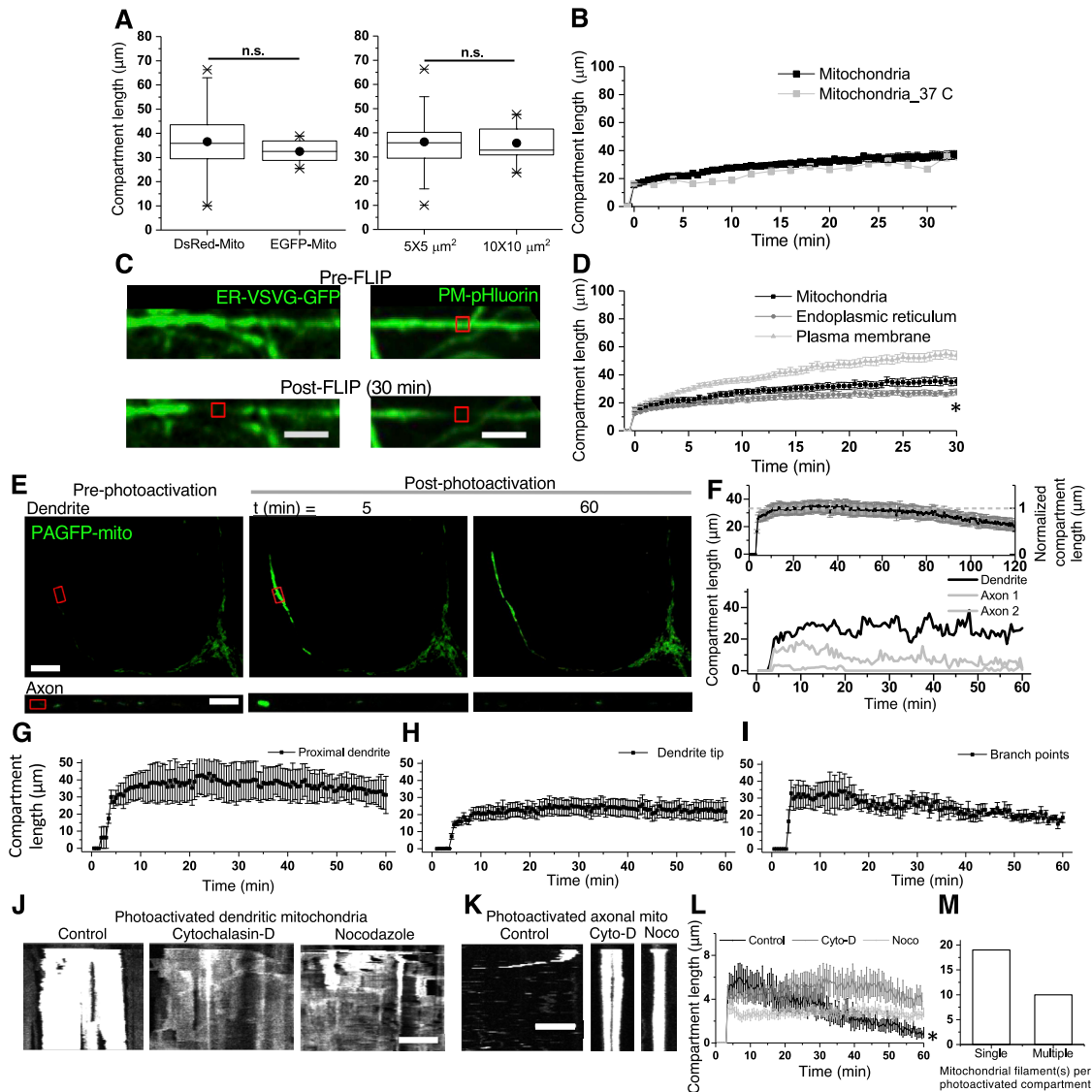
Figure S2. Mitochondrial Compartment Stability in Dendrites, but Not in Axons, Is Achieved by Local Cytoskeletal-Tethering, Related to Figure 2

(A) Mitochondrial compartment lengths measured in dendrites and somata were not influenced by either the fluorescent reporter used to measure FLIP (left, n ≥ 6 neurons from 7 animals), or by increasing the size of the FLIP region (right, n ≥ 9 neurons from 8 animals), One-Way ANOVA, Tukey test. p > 0.4

(B) The observed stability of the mitochondrial compartments in control conditions (black, n = 25 dendrites from 6 animals) was not affected at physiological temperatures (37°C) (gray, n = 16 dendrites from 1 animal) during 30 min of FLIP. Two-sample t test at 32 min, p = 0.2.

(C) Hippocampal neuron expressing endoplasmic reticulum targeted GFP (ER-VSVG-GFP, green) (left) or plasma membrane targeted pHluorin (PM-pHluorin, green) (right) before (top) and after (bottom) 30 min FLIP at a proximal dendritic region (red open square). Scale bar = 20 μm.

(D) Simultaneous FLIP imaging of mitochondria along with endoplasmic reticulum revealed that the measured mitochondrial compartment lengths (black, n = 30 dendrites from 3 animals) is distinct from endoplasmic reticulum compartments (gray, n = 27 dendrites from 3 animals) at 30 min of FLIP, One-Way ANOVA, Tukey test, *p < 0.05. However, FLIP imaging of plasma membrane did not reveal a stable compartment (light gray, n = 8 dendrites from 1 animal).

(E) Mitochondrial compartments photoactivated (red rectangle) at the proximal dendritic region (top) in photoactivatable GFP (PAGFP-mito, green) expressing hippocampal neurons were stable and resident in the same region for up to 60 min, but not in axons (bottom). Scale bar = 10 μm.

(F–I) (top) Average time course of the photoactivated mitochondrial compartment lengths showed stable mitochondrial compartments till ∼80 min of imaging but their stability reduced by 40% (decrease in compartment length) at 120 min. Dashed gray line represents the average compartment length measured between 20 and 60 min that was used for normalization. (bottom) Representative time course of the photoactivated mitochondrial compartment lengths show stable mitochondria in dendrites (black) but not in axons (gray). Average time course of photoactivated mitochondrial compartment lengths measured at various dendritic regions show stable mitochondria in proximal dendrites (G, n = 4 from 4 animals) and dendritic tips (H, n = 11 from 4 animals) but not at branch points (I, n = 3 from 2 animals).

(J) Representative kymographs of photoactivated mitochondrial compartments showed stable mitochondrial compartments in control dendrites (left), but de-stabilized and shortened mitochondrial compartments following actin (Cytochalasin-D, middle) and microtubule depolymerization (Nocodazole, right). Scale bar = 10 μm; vertical length = 60 min.

(K) Representative kymographs of photoactivated mitochondria showed dynamic mitochondria in control axons (left), but stabilization of mitochondria on depolymerization of actin (middle, cyto-D) and microtubule (right, noco). Scale bar = 10 μm; vertical length = 60 min.

(L) Average time course of the photoactivated mitochondrial compartment lengths did not show stable mitochondria in control axons (black, n = 12 axons from 1 animal), but stabilized mitochondria were observed following actin (dark gray, n = 17 axons from 1 animal) and microtubule (light gray, n = 12 axons from 1 animal) depolymerization. Paired-sample t test (control t = 5 min, t = 60 min, *p < 0.005; cyto-D t = 5 min, t = 60 min, p = 0.7; noco t = 5 min, t = 60 min, p = 0.4).

(M) Quantification of single and multiple mitochondrial filaments in photoactivated mitochondrial compartments (n = 29 dendrites from 4 animals).
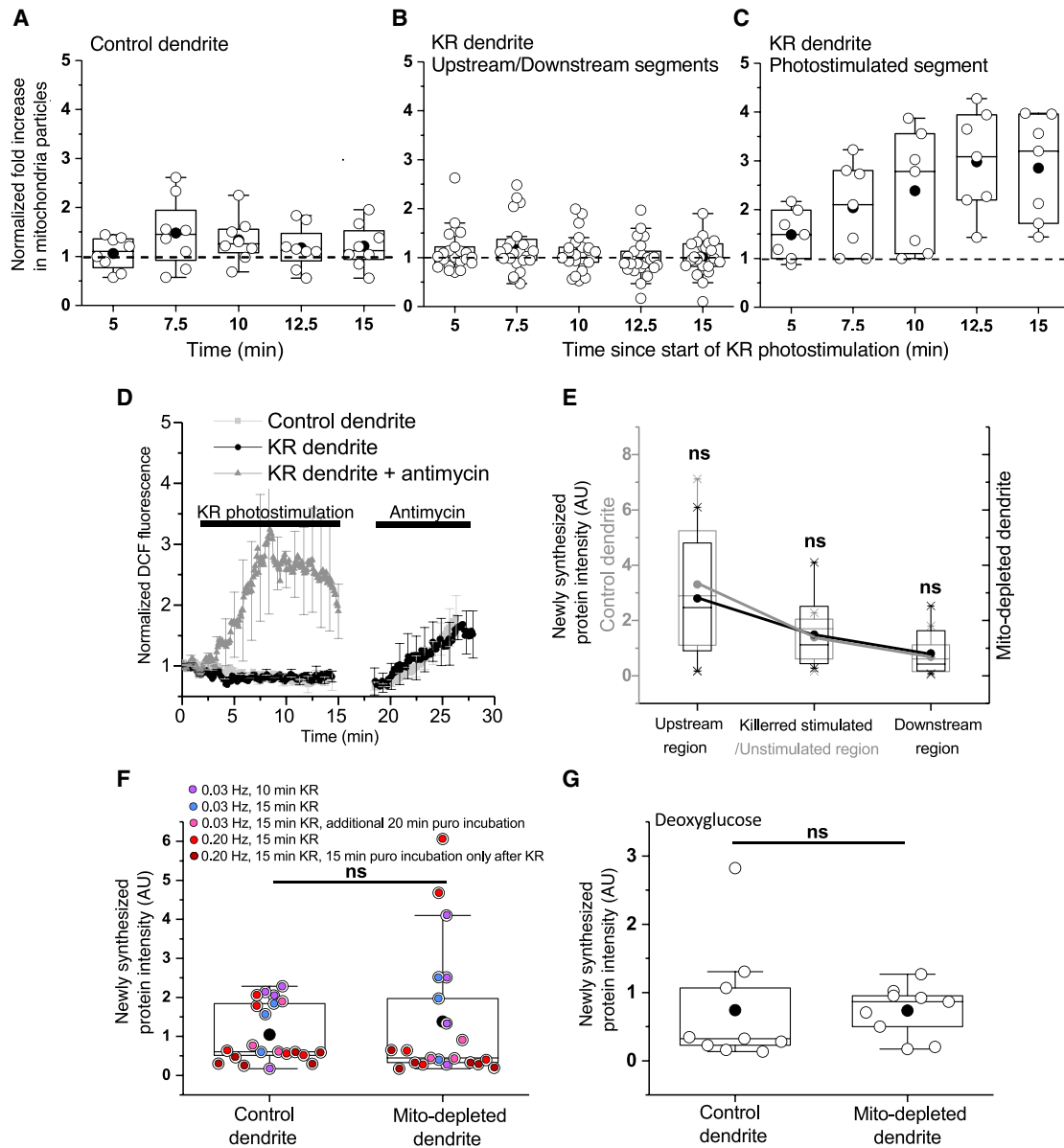
Figure S3. Local Inhibition of Mitochondrial Compartments Is Not Toxic and Does Not Affect Local Translation during Basal Neuronal Activity, Related to Figure 3

(A–C) Mitochondrial fragmentation measured by the fold increase in number of mitochondria particles was not observed in non-KR photostimulated control dendrites (A), nor upstream and downstream segments of the KR photostimulated segment (B), mitochondrial fragmentation was only observed in KR-photo-stimulated dendritic segments (C) (see STAR Methods), $n \geq 7$ dendrites from 3 animals. Black dashed line represents the control condition corresponding to an absence of mitochondrial fragmentation.

(D) DCF fluorescence measuring cytosolic reactive oxygen species (ROS) levels did not show an increase during local KR photostimulation of mitochondria, in comparison to the marked increase in cytosolic ROS levels observed following antimycin treatment as a positive control, n = 3 dendrites from 2 animals (see STAR Methods). The slight decrease in DCF fluorescence during KR photostimulation (black, n = 7 dendrites from 2 animals) is attributed to photobleaching, and is not observed in control dendrites (light gray, n = 8 dendrites from 2 animals). Addition of antimycin during the KR photostimulation period (gray, n = 4 dendrites from 2 animals) also showed an increase in DCF fluorescence indicating that the local photobleaching of DCF during KR photostimulation doesn't affect its ability to respond to increase in ROS levels, if any. The lack of DCF fluorescence increase in our KR photostimulation experiments suggest an absence of any significant ROS generation in the cytosol.
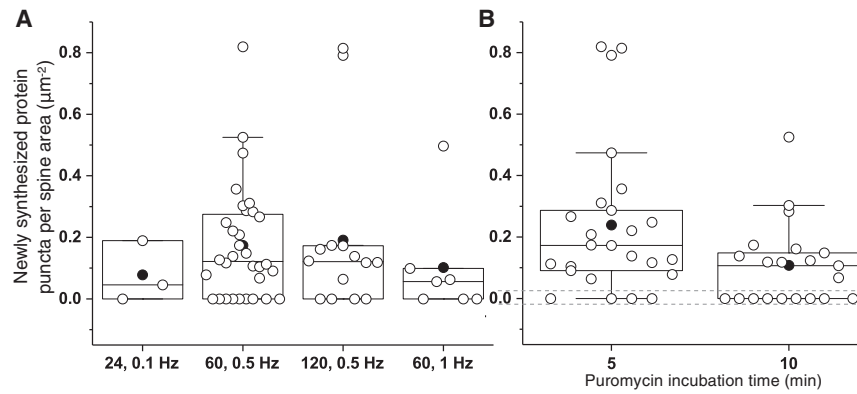
(E–G) (E) Average newly synthesized protein intensity measured in mitochondria depleted-dendritic regions (Killerred stimulated region, black) showed no change compared to the adjacent non-photostimulated regions (Upstream and Downstream regions, black) of the respective dendrites. Average newly synthesized protein intensity measured in control dendrites at the same distance from the soma, as in the mitochondria-depleted dendrite, was used as negative control

(legend continued on next page)

(Upstream, Unstimulated and Downstream regions, gray), n = 10 dendrites from 4 animals, Paired-sample t test, p > 0.1. Average newly synthesized protein intensity measured pairwise in non-KR photostimulated control dendrites and KR photostimulated-mitochondria depleted dendrites (F) at various KR photostimulation conditions (see STAR Methods), n = 21 dendrites from 6 animals, Paired-sample t test, p = 0.2 (note that data are taken from Figure 3C) and (G) in the presence of Deoxyglucose, n = 9 dendrites from 3 animals, Paired-sample t test, p = 1.

Figure S4. Optimization of Glutamate Uncaging Protocol for Visualization of Nascent Proteins in Spines, Related to Figure 4

(A) Average number of newly synthesized protein puncta normalized to spine area measured at spines stimulated with different uncaging pulses, n ≥ 3 spines from 14 animals. 0.5 Hz showed a higher success rate of newly synthesized proteins (72%) per spine area on glutamate uncaging compared to the other two frequencies (0.1 Hz - 67% and 1 Hz - 57%).

(B) Average number of newly synthesized protein puncta normalized to spine area measured at stimulated spines with reduced wait time following uncaging stimulus until fixation (5 min) showed a higher success rate (84%) of synaptic translation compared to longer wait times (10 min, 57% success rate) n ≥ 21 spines from 12 animals.
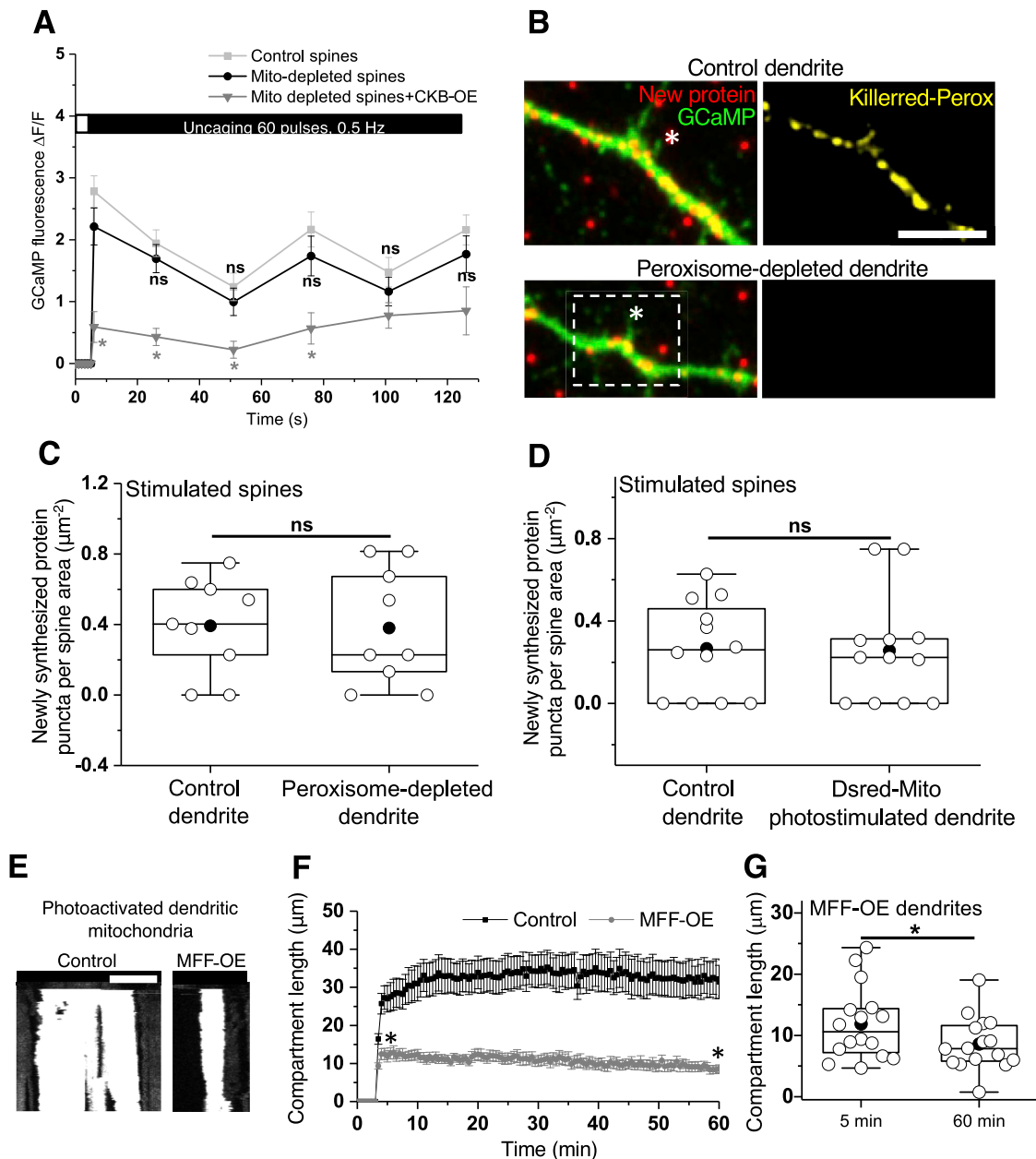
Figure S5. Control Experiments Related to Killered Photostimulation, Related to Figure 5

(A) GCaMP calcium response measured in control spines (light gray) and KR photostimulated-mitochondria depleted spines (black) during uncaging pulses were largely not significantly different from each other. n = 35 spines from 15 animals, Paired-sample t test, p = 0.05 (at 6 s); 0.3 (at 25 s); 0.3 (at 50 s); 0.2 (at 75 s); 0.2 (at 100 s); and 0.1 (at 125 s); GCaMP calcium response measured in KR photostimulated-mitochondria-depleted spines in the presence of CKB-OE (gray) was significantly reduced compared to control spines n = 10 spines from 4 animals, Two-sample t test, *p < 0.0005 (at 6 s); *p < 0.0005 (at 25 s); *p < 0.005 (at 50 s); *p < 0.05 (at 75 s); p = 0.2 (at 100 s); p = 0.08 (at 125 s). Error bars indicate SEM.

(B) Local photostimulation of KR targeted to the peroxisome (Killerred-Perox, yellow) did not affect synaptic translation (new protein, red) in stimulated spines (*) and was comparable to stimulated spines (*) in non-KR photostimulated control dendrites. Scale bar = 10 μm.

(C) Average newly synthesized protein puncta normalized to spine area measured in stimulated spines of non-KR photostimulated control dendrites and peroxisome-depleted dendrites were comparable. n = 9 spines from 4 animals, Paired-sample t test, p = 0.9.

(D) Average newly synthesized protein puncta normalized to spine area measured in stimulated spines of non-KR photostimulated control dendrites and Dsred-Mito photostimulated dendrites were comparable. n = 12 spines from 4 animals, Paired-sample t test, p = 0.9.

(E) Representative kymographs of photoactivated mitochondrial compartments showed stable mitochondrial compartments in control dendrites (left, note that image is taken from Figure S2J, control), but shortened and modestly destabilized mitochondrial compartments in MFF-OE dendrites (right). Scale bar = 10 μm; vertical length = 60 min.

(F) Average time course of the photoactivated mitochondrial compartment lengths in MFF-OE dendrites showed reduced mitochondrial compartment length (gray, n = 16 dendrites from 1 animal) compared to control (WT) dendrites (Black, n = 18 dendrites from 1 animal, note that data are taken from Figure 2D, control dendrites). One-Way ANOVA, Tukey test, control and MFF-OE dendrites *p < 0.0005.

(G) Shortened mitochondrial compartments measured in MFF-OE dendrites showed a modest but reduced stability. n = 16 dendrites from 1 animal, Paired-sample t test, MFF-OE at 5 and 60 min. *p < 0.005.
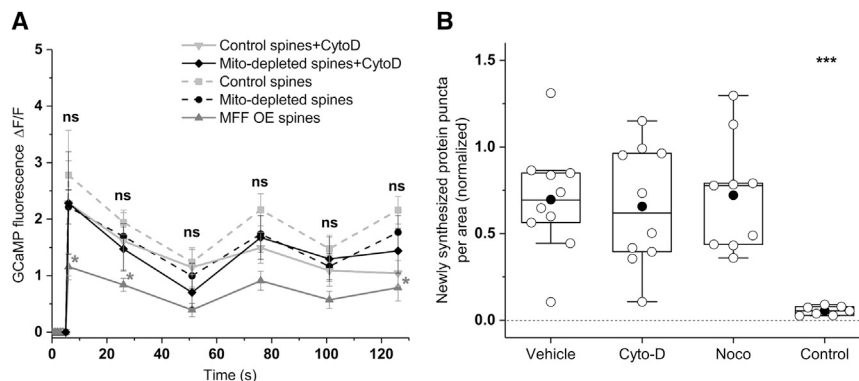
Figure S6. Control Experiments Related to Cyto-D/Noco and MFF-OE Experiments, Related to Figure 6

(A) GCaMP calcium response measured in control spines treated with cyto-D (light gray) and KR photostimulated-mitochondria depleted spines treated with cyto-D (black) during uncaging pulses were not significantly different from control spines (dashed light gray, note that data are taken from Figure S5A, control spines) and KR photostimulated-mitochondria depleted spines (dashed black, note that data are taken from Figure S5A, Mito-depleted spines) respectively. n ≥ 5 spines from 17 animals, Two-sample t test, p ≥ 0.5 (at 6 s); 0.4 (at 25 s); 0.4 (at 50 s); 0.5 (at 75 s); 0.8 (at 100 s); and 0.3 (at 125 s); GCaMP calcium response measured in MFF-OE spines (gray) was significantly reduced compared to control spines. n ≥ 18 spines from 17 animals, Two-sample t test, p = 0.02 (at 6 s); 0.01 (at 25 s); 0.07 (at 50 s); 0.08 (at 75 s); 0.09 (at 100 s); and 0.03 (at 125 s). Error bars indicate SEM.

(B) Average number of newly synthesized protein puncta normalized to area measured in dendrites treated with Cytochalasin-D (cyto-D) and nocodazole (noco) for 20 min showed no effect on basal protein synthesis compared to vehicle. Absence of puromycin was used as negative control (control). n ≥ 7 neurons from 1 animal, One-Way ANOVA, Tukey test, p = 0.9. Note the decrease in the newly synthesized protein puncta per area with decrease in the metabolic labeling period, here 5 min (see also Figures 1D, 1E, S1A, and S1B).